nature structural & molecular biology

Article

https://doi.org/10.1038/s41594-023-01176-4

# Structural basis of prostaglandin efflux by MRP4

Received: 21 December 2022

Accepted: 7 November 2023

Sergei Pourmal[1,2,8], Evan Green[1,3,9,11], Ruchika Bajaj[4,11], Ilan E. Chemmama[4,10], Giselle M. Knudsen[5], Meghna Gupta[1], Andrej Sali[4,5,6], Yifan Cheng[1,7], Charles S. Craik[6], Deanna L. Kroetz[4] ✉ & Robert M. Stroud[1] ✉

Multidrug resistance protein 4 (MRP4) is a broadly expressed ATP-binding cassette transporter that is unique among the MRP subfamily for transporting prostanoids, a group of signaling molecules derived from unsaturated fatty acids. To better understand the basis of the substrate selectivity of MRP4, we used cryogenic-electron microscopy to determine six structures of nanodisc-reconstituted MRP4 at various stages throughout its transport cycle. Substrate-bound structures of MRP4 in complex with $PGE_1$, $PGE_2$ and the sulfonated-sterol DHEA-S reveal a common binding site that accommodates a diverse set of organic anions and suggest an allosteric mechanism for substrate-induced enhancement of MRP4 ATPase activity. Our structure of a catalytically compromised MRP4 mutant bound to ATP-$Mg^{2+}$ is outward-occluded, a conformation previously unobserved in the MRP subfamily and consistent with an alternating-access transport mechanism. Our study provides insights into the endogenous function of this versatile efflux transporter and establishes a basis for MRP4-targeted drug design.

The prostanoid family of lipid mediators are signaling molecules involved in processes as diverse as inflammation, nociception, immune response, vasoactivity and parturition[1–7]. Prostanoids are derived from the cyclooxygenase-mediated metabolism of unsaturated fatty acids and subsequently converted in a tissue-specific manner into prostaglandins or thromboxanes[8]. Acting in an autocrine or paracrine fashion, secreted prostanoids activate their cognate G-protein-coupled receptors, leading to modulation of intracellular $Ca^{2+}$ or cAMP levels that affect downstream signaling and gene expression. Altered prostanoid signaling has implications for a variety of pathologies, including thrombosis, blood pressure, gastrointestinal cancers and regulation of the tumor microenvironment[9–11]. Synthetic prostaglandins have clinical use for induction of labor and abortions, treatment of glaucoma and pulmonary hypertension, vasodilation and the prevention of stomach ulcers[12–16]. Despite the numerous physiological roles of prostanoids and the therapeutic potential of their analogs, structural details on their transport from the cell remain limited.

The efflux of prostaglandins is mediated by MRP4 (ref. 17). Broadly expressed in tissues including the liver, kidneys, blood–brain barrier and blood cells, MRP4 is a membrane bound ATP-binding cassette (ABC) transporter from the MRP family (a subgroup within the ABCC family) that acts as a unidirectional efflux pump. It is classified as a type IV exporter, containing two transmembrane domains (TMDs) and two nucleotide-binding domains (NBDs) within a single polypeptide chain[18] (Fig. 1a). It is the only member of the MRP subfamily that has an established role in the transport of prostanoids, including $PGE_1$, $PGE_2$,

---

[1]Department of Biochemistry and Biophysics, University of California, San Francisco, CA, USA. [2]Program in Chemistry and Chemical Biology, University of California, San Francisco, CA, USA. [3]Biophysics Graduate Program, University of California, San Francisco, CA, USA. [4]Department of Bioengineering and Therapeutic Sciences, University of California, San Francisco, CA, USA. [5]Quantitative Biosciences Institute, University of California, San Francisco, CA, USA. [6]Department of Pharmaceutical Chemistry, University of California, San Francisco, CA, USA. [7]Howard Hughes Medical Institute, University of California, San Francisco, CA, USA. [8]Present address: Genentech, South San Francisco, CA, USA. [9]Present address: Exelixis, Alameda, CA, USA. [10]Present address: Brightseed, South San Francisco, CA, USA. [11]These authors contributed equally: Evan Green, Ruchika Bajaj. ✉e-mail: kroetz.3@osu.edu; stroud@msg.ucsf.edu

$PGD_2$, $PGF_{2\alpha}$ and $TXB_2$ (refs. 17,19,20). Among these, $PGE_2$ is of interest as the most abundant prostanoid in humans and has been implicated in cancer pathology by promoting tumor growth, metastasis and immune evasion[9,11,21]. Consistent with a role for MRP4 in pathological prostaglandin efflux, its overexpression in breast tumors has been associated with poor prognosis[22], suggesting therapeutic potential in modulating MRP4 function.

In addition to prostaglandin efflux, MRP4 is associated with transporting a variety of structurally diverse substrates. It overlaps with other MRPs in the transport of steroid conjugates, including dehydroepiandrosterone sulfate (DHEA-S), the steroid with the highest circulating concentration in humans and a precursor for androgens and estrogens[23]. MRP4 has been classified as a cyclic nucleotide transporter[24], as studies in *Mrp4*$^{-/-}$ (also known as *Abcc4*$^{-/-}$) mice have linked cyclic nucleotide transport by MRP4 to vascular reactivity and resistance to hypoxic pulmonary hypertension[25], impaired platelet activation[26] and cystic fibrosis transmembrane conductance regulator-mediated chloride flux and secretory diarrhea[27,28]. Other substrates of MRP4 include cysteinyl leukotrienes, bile salts, folate, sphingosine-1-phosphate, cephalosporin antibiotics and antivirals[23,29–37], although these substrates have only been identified through overexpression systems.

To understand the molecular details of MRP4 function and to identify the structural elements that define the substrate selectivity of the transporter, we determined six structures of MRP4 in various conformations using cryogenic-electron microscopy (cryo-EM), including nucleotide- and substrate-free (apo$_{\mathrm{wide}}$ and apo$_{\mathrm{narrow}}$), substrate-bound (DHEA-S, $PGE_1$ and $PGE_2$) and ATP-bound states. Our substrate-bound structures provide insights into substrate discrimination among MRPs, while our ATP-bound MRP4$_{\mathrm{E1202Q}}$ structure expands our understanding of the ABCC family conformational landscape by revealing the outward-facing occluded state, an important intermediate in the proposed alternating-access mechanism of substrate translocation. These structures will enable computational studies into the role of MRP4 in transporting xednobiotic and endogenous substrates and provide a basis for designing molecules modulating MRP4-mediated efflux.

## Results

### Functional characterization of MRP4

*Bos taurus* MRP4, which has 90% similarity to human MRP4 (Extended Data Fig. 1), was heterologously expressed in *Spodoptera frugiperda* (Sf9) cells with a C-terminal 8-His tag. Following detergent solubilization, we reconstituted MRP4 into MSP E3D1 nanodiscs to facilitate ATPase activity assays and cryo-EM structure determination within a native lipid environment. Nanodiscs were assembled while MRP4 was bound to TALON resin, yielding efficient incorporation of the transporter (Fig. 1b).

As some type IV exporters display substrate-dependent increases in ATPase activity[38–40], we used the stimulation of MRP4 ATP hydrolysis to assess previously identified substrates. MRP4 was determined to have a Michaelis constant ($K_m$) for ATP of 0.60 mM (95% confidence interval (CI) 0.47–0.77 mM) and maximum reaction rate ($V_{\max}$) of 19.7 nmol min$^{-1}$ mg$^{-1}$ (95% CI 18.4–21.1 nmol min$^{-1}$ mg$^{-1}$) (Fig. 1c) in the absence of substrates. These are similar to previously reported values for human MRP4 (ref. 41) and correspond to a turnover number of 4.1 min$^{-1}$ (95% CI 3.8–4.4 min$^{-1}$). $PGE_1$, $PGE_2$ and DHEA-S (Fig. 1f) stimulated the ATPase activity of MRP4 in a concentration-dependent manner, whereas other known substrates, including the cyclic nucleotides cAMP and cGMP and the MRP1 substrate leukotriene $C_4$ ($LTC_4$)[18,42] did not (Fig. 1d, Extended Data Table 1 and Extended Data Fig. 2). As these results indicated the presence of high-affinity transporter–substrate complexes, we pursued structures of MRP4 bound to these three ATPase-stimulating substrates.

ATP binding typically induces NBD dimerization in ABC transporters. The two nucleotide-binding sites (NBS) are located at the interface

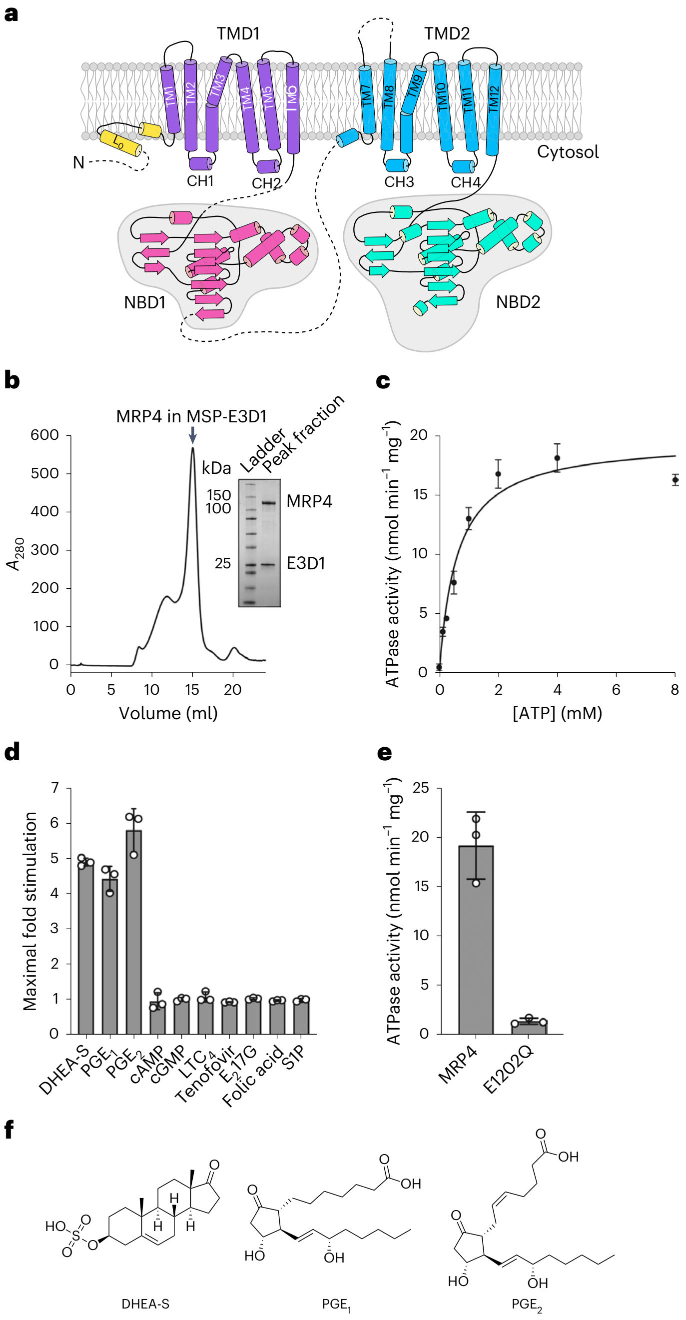

**Fig. 1 | Functional characterization of MRP4 and identification of three stimulating substrates. a**, Schematic illustration of the domain architecture of MRP4 with residue numbers at domain boundaries indicated. $L_0$ N-terminal loop domain, yellow; TMD1, purple; NBD1, pink; TMD2, blue; and NBD2, cyan. **b**, Representative gel filtration chromatography profile of wild-type (WT) MRP4 embedded into MSP E3D1 lipid nanodiscs. SDS–PAGE analysis of peak fraction is inserted on the right, visualized by Coomassie brilliant blue staining. Gel electrophoresis was performed once ($n = 1$). **c**, ATPase activity of nanodisc embedded MRP4. Data are the mean ± s.d. for three technical replicates from a single MRP4 preparation and fit to the Michaelis–Menten equation. **d**, Stimulation of wild-type MRP4 ATPase activity at 4 mM ATP in the presence of previously reported substrates. Stimulation data are shown for the highest concentration tested of a given substrate and are mean ± s.d. for three technical replicates from a single MRP4 preparation. S1P, sphingosine-1-phosphate. **e**, Comparison of wild-type MRP4 and MRP4$_{\mathrm{E1202Q}}$ ATPase activity in lipid nanodiscs. Data are mean ± s.d. for three technical replicates from a single preparation each of MRP4 and MRP4$_{\mathrm{E1202Q}}$. **f**, Structures of previously reported transport substrates found to stimulate MRP4 ATPase activity.

of the NBDs, formed by the interaction of the A-, Q- and H-loops and Walker A and B motifs from one NBD, with the signature sequence and X-loop from the other. In MRP4, sequence analysis (Fig. 4a and Extended Data Fig. 1) reveals that the NBD2 Walker B motif contributes a catalytic E1202 to NBS2, forming an active ATP-hydrolysis site. The residue in the corresponding position of the NBD1 Walker B motif is D560 that suggests, along with other deviations from consensus motifs in NBS1, that the noncanonical NBS1 has impaired catalytic activity[43]. To trap MRP4 in a nucleotide-bound state, we introduced a mutation ($MRP4_{E1202Q}$) designed to disrupt ATP hydrolysis at NBS2 while retaining the capacity of the site to bind nucleotides. $MRP4_{E1202Q}$ showed negligible ATPase activity, consistent with a role for E1202 in ATP hydrolysis (Fig. 1e).

### Structures of MRP4 along the substrate transport cycle

MRP4 in lipid nanodisc was purified and frozen under various conditions for cryo-EM analysis. Our apo dataset revealed a heterogenous sample with fluctuations in the angle between the two halves of the transporter, resulting in reconstructions of two distinct conformations, $apo_{wide}$ and $apo_{narrow}$, at 3.3 Å (Fig. 2a, Table 1 and Supplementary Figs. 1 and 2). MRP4 in the presence of DHEA-S, $PGE_1$ or $PGE_2$ yielded reconstructions at 2.7, 3.5 or 2.9 Å, respectively, each showing clear densities for the substrates bound to MRP4 (Fig. 2b–d and Supplementary Figs. 3–5). A final dataset was collected for $MRP4_{E1202Q}$ under saturating ATP-$Mg^{2+}$ conditions, with $PGE_2$ added to accelerate progression through the transport cycle. This experiment resulted in a 3.1 Å map with density observed for ATP-$Mg^{2+}$ but not for $PGE_2$ (Fig. 2e and Supplementary Fig. 6). We refined our models into their respective densities, which together reveal four distinct conformations of MRP4.

A dataset was collected for MRP4 in the presence of cAMP, which failed to enhance MRP4 ATPase activity in vitro despite reports of cAMP transport by MRP4 in various cell types and membrane-derived vesicles[24,44]. Cryo-EM analysis of MRP4 with 1 mM cAMP (a concentration higher than previously reported $K_m$ values and cytoplasmic levels) revealed a structure at 3.7 Å, with no conformational change relative to $apo_{wide}$ MRP4 (Extended Data Fig. 3a,b) and no density observed for cAMP (Extended Data Fig. 3c). The structure of MRP4 in this condition was not modeled.

The overall architecture of MRP4 is composed of two halves, each consisting of a TMD–NBD pair. The two halves are configured in a pseudo-two-fold symmetric arrangement perpendicular to the membrane, with an 82-residue linker connecting NBD1 and TMD2; this linker remains unresolved in all six structures. Both TMDs domain-swap a pair of helices between each other, so that TM1, TM2, TM3, TM6, TM10 and TM11 form one distinct transmembrane bundle and TM4, TM5, TM7, TM8, TM9 and TM12 form another (Fig. 2a–e). The lasso motif, an N-terminal feature of the ABCC family, contains a membrane-embedded helix that packs against TM3, TM10 and TM11 and a second extended helix that runs parallel to the inner leaflet of the membrane[45]. The N-terminal portions of the lasso motif were only resolved in the DHEA-S and $PGE_1$-bound structures.

### Substrates and ATP induce conformational changes in MRP4

Both the $apo_{wide}$ and $apo_{narrow}$ structures of MRP4 are in an inward-facing conformation. Between the two transmembrane bundles, a solvent-filled cavity (roughly 11,000 $Å^3$ in $apo_{wide}$ and 10,000 $Å^3$ in $apo_{narrow}$) extends from the cytoplasm into the lipid bilayer. It concludes at the interface of the bundles and the site of substrate binding. In $apo_{wide}$, the bundles are at their maximal observed separation and the substrate-binding site is accessible, characterized by a 16.7 Å distance between the backbone $C_\alpha$ of a pair of substrate-binding residues (F211 from TM3 in TMD1 and W995 from TM12 in TMD2) (Fig. 3a). The NBDs in $apo_{wide}$ are separated from one another by an estimated 27 Å at either of the two NBSs (Fig. 3b), as measured by the $C_\alpha$ distance between the signature sequence serine of one NBD and the Walker A glycine of the other NBD. While $apo_{narrow}$ MRP4 is largely unchanged from $apo_{wide}$ in the transmembrane regions (Fig. 3a), the distance between residues at either NBS decreases to an estimated 23 Å (Fig. 3b), demonstrating subtle conformational fluctuations in the absence of substrate or nucleotides.

On substrate binding, MRP4 undergoes a clamshell-like closure, reducing the angle between the two transmembrane bundles by 20° compared to $apo_{narrow.}$ This movement constricts the central cavity (to approximately 5,400 $Å^3$) while keeping it open toward the cytoplasm (Fig. 3a). More pronounced conformational changes occur in the distal cytoplasmic regions of MRP4, where the NBDs approach each other and are now askew (Fig. 3b). These changes are consistent on binding to any of the three ATPase-stimulating substrates; the highest root-mean-square deviation between the three substrate-bound structures is 1.2 Å, suggesting our structures represent a common substrate-bound state (Extended Data Fig. 4).

In the presence of ATP and $PGE_2$, $MRP4_{E1202Q}$ undergoes notable structural changes. In the cytoplasm, the NBDs are dimerized with two copies of ATP-$Mg^{2+}$ at their interface. The TMDs align in an orientation that closes off the central cavity from the cytoplasm and alters the substrate-binding site to prevent substrate binding (Fig. 3a,b). The lack of observed $PGE_2$ density in the ATP-bound $MRP4_{E1202Q}$ map suggests that closure of the soluble cavity follows substrate transport across the membrane.

The extracellular surface of MRP4 remains closed in all states (Fig. 3c), with hydrophobic residues packing to form an extracellular gate that seals the interface of the two TMDs. The presence of this closed gate in our ATP-bound structure suggests that the substrate exit pathway at the extracellular face can reset independent of ATP hydrolysis and NBD dissociation, possibly to maintain unidirectional transport. Throughout the substrate transport cycle of MRP4, the two halves of the transporter move as rigid bodies, showing only minor rearrangements within the TMDs or NBDs (Extended Data Fig. 4).

### MRP4 NBDs bind nucleotides through canonical interactions

The interface between the TMDs and NBDs connects substrate transport to ATP hydrolysis. As in other type IV architectures, a pair of coupling helices in the loops between the domain-swapped TM4, TM5, TM10, and TM11 fit into a shallow cleft in either NBD (Fig. 4b,c). Compared to NBD1, NBD2 contains an insertion of 13 residues between the Walker A motif and the signature sequence (Fig. 4a). These residues (1099–1111) form two short helices that cap the distal end of the NBD2 cleft and tightly pack with the linker between TM12 and NBD2 (Fig. 4c). H1111 from the second inserted helix hydrogen bonds with E292 from TM5 while simultaneously forming π–π interactions with W1025 from the TM12-NBD2 linker. A turn of the helix away, R1114 forms a salt bridge with E1022, further stabilizing contact with the linker (Fig. 4d). The absence of a corresponding region in NBD1 results in a smaller interface and fewer contacts with the cytoplasmic extensions of transmembrane helices TM2, TM3, TM10 and TM11 (Fig. 4b), and potentially contributes to the flexibility and lower local resolution observed in this domain across the apo- and substrate-bound datasets (Supplementary Figs. 1f, 2f, 3f, 4f and 5f).

In the ATP-bound $MRP4_{E1202Q}$ structure, clear densities define ATP-$Mg^{2+}$ in both the noncanonical NBS1 and in the mutated NBS2 (Supplementary Fig. 6b). Nucleotide binding in either site is mediated by highly conserved features, including electrostatic interactions between $Mg^{2+}$ and the Walker A motif (K451 and K1081), and between phosphates and the Walker B motif (D560 and E1202Q), Q-loop (Q480 and Q1122), H-loop (H592 and H1233) and the signature sequence (S1178 and S536) (Fig. 4e,f). In both NBSs, A-loop aromatic residues (W419 and Y1050) form π–π interactions with the adenine rings of ATP (Fig. 4e,f), while residues from CH1 and CH3 (N183 and D812) coordinate the exocyclic amines.

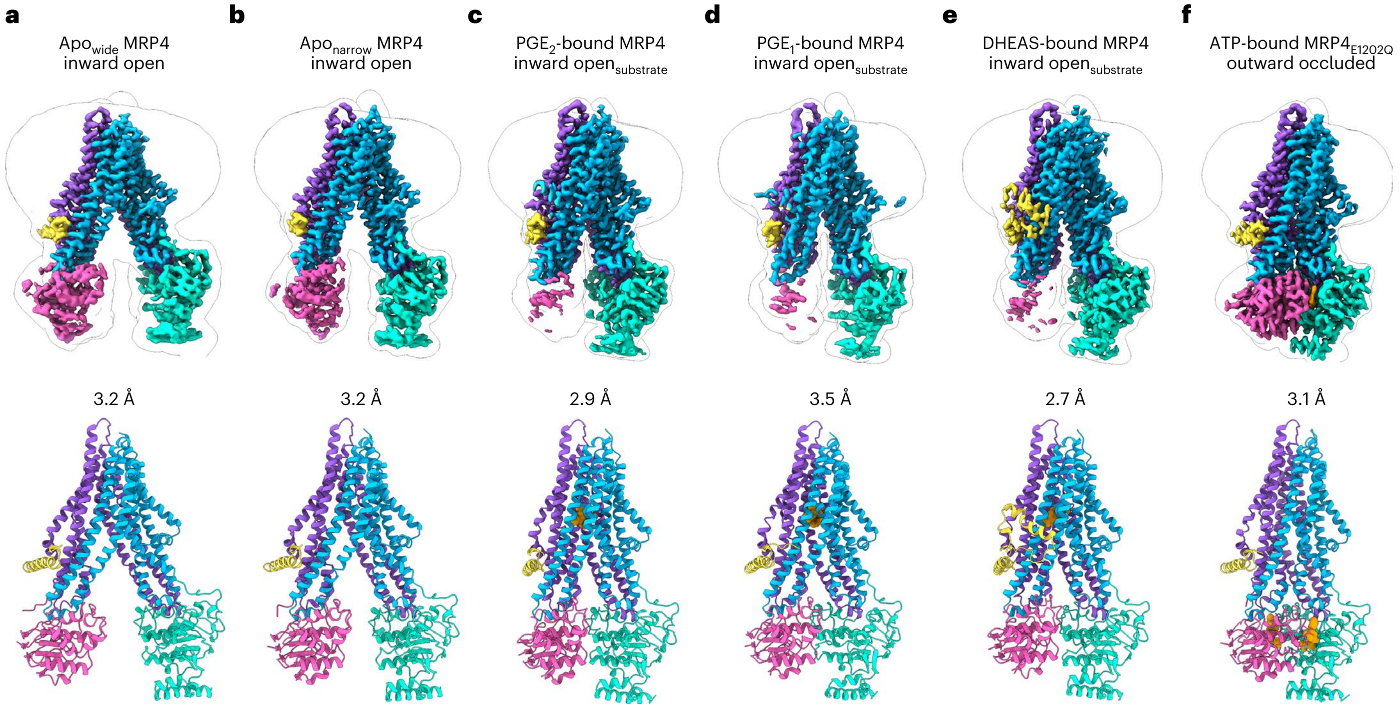

**Fig. 2 | Structures of MRP4 in multiple conformations along the substrate transport cycle.** **a**–**f**, Side views of the cryo-EM reconstruction and atomic model of inward-open $\mathrm{apo}_{\mathrm{wide}}$ conformation of MRP4 (**a**), inward-open $\mathrm{apo}_{\mathrm{narrow}}$ conformation of MRP4 (**b**), $PGE_2$-bound MRP4, inward-$\mathrm{open}_{\mathrm{substrate}}$ (**c**), $PGE_1$-bound MRP4, inward-$\mathrm{open}_{\mathrm{substrate}}$ (**d**), DHEA-S-bound MRP4, inward-$\mathrm{open}_{\mathrm{substrate}}$ (**e**) and outward-occluded, ATP-$Mg^{2+}$-bound $\mathrm{MRP4}_{\mathrm{E1202Q}}$ (**f**). The sharpened electrostatic potential maps shown were generated using DeepEMhancer. Domains in sharpened maps and models are colored as in Fig. 1a. A transparent low-pass filtered envelope depicts density for the nanodisc and poorly resolved portions of the NBDs. Membrane boundaries are represented by cartoon. $PGE_2$, $PGE_1$, DHEA-S and ATP-$Mg^{2+}$ are shown as orange spheres in their respective structures. $A_{280}$, absorbance at 280 nm.

The nucleotide density in either NBS is continuous between the β and γ phosphates, suggesting $\mathrm{MRP4}_{\mathrm{E1202Q}}$ prevents the transporter from progressing through the ATPase cycle. The 7.1 Å separation between the terminal carboxyl of D650 and the phosphorus of the γ phosphate of ATP in NBS1 is greater than the 4.3 Å distance between the amide of the mutated E1202Q and the equivalent phosphorus in NBS2. This increased separation may compromise the ability of D560 to activate a lytic water for ATP hydrolysis and potentially lower the rate of catalysis at NBS1, as observed in MRP1 (ref. 46).

## The amphipathic substrate-binding site of MRP4

$PGE_1$ and $PGE_2$ stimulate MRP4 ATPase activity. Both are composed of 20 carbon atoms, organized as a cyclopentanone core (C8–C12) with two alkyl chain substituents (the α chain, C1–C7 and ω chain, C13–C20) (Fig. 1f). $PGE_1$ differs from $PGE_2$ by the saturation of a second carbon–carbon double bond at C5, and both substrates share a similar pose when bound to MRP4. $PGE_1$ and $PGE_2$ bind MRP4 in the solvent-accessible central cavity, engaging residues from both TMD1 and TMD2. The binding site is a narrow channel composed of a large hydrophobic region and pockets of charged residues that coordinate the polar groups of the substrate (Fig. 5b).

In both prostaglandin-bound structure, the alkyl chains and the cyclopentanone core are wedged between W995 on TMD2 and a hydrophobic patch on TMD1 formed by F156, F211, F324, L363, L367 and F368. The shared polar substituents of $PGE_1$ and $PGE_2$ further orient the substrates. Specifically, the C1 carboxyl sits in a positively charged pocket (P-site 1) composed of H152 and Q160 from TM2, R946 from TM11, and R998 and Q994 from TM12. The C9 ketone and the C11 hydroxyl point toward a narrow solvent-accessible cavity that extends above the substrates toward the extracellular face of MRP4, while the C15 hydroxyl of either prostaglandin faces a pocket on TM9 formed by D842, Q845 and T846. Collectively, the hydrophobic core, the α chain carboxyl and the C9, C11 and C15 substituents allow MRP4 to bind and translocate these prostaglandins specifically.

In addition to these two prostanoids, we found that the steroid DHEA-S also stimulated MRP4 ATPase activity. The sterol core of DHEA-S is conjugated by a sulfate ester at the 3β position and has a ketone on C17, providing polar groups at either end of the aliphatic sterol core for electrostatic interactions. MRP4 binds DHEA-S in the same site as $PGE_1$ and $PGE_2$, using residues from both TMD1 and TMD2. The binding site residues in all three substrate-bound structures adopt similar rotamers, indicating a common substrate-bound state.

The 17-ketosteroid backbone of DHEA-S makes extensive van der Waals contacts with the hydrophobic patch on TMD1 through its β face. L363, L367 and F368 intercalate between the two methyl substituents of DHEA-S, while F156, F211 and F324 pack against the periphery of the sterol core. W995 from TM12 stacks against the α face of DHEA-S, and the indole ring of W995 hydrogen bonds with the carboxyl of D842. The ketone moiety of the steroid and an ordered water occupy P-site 1. Elsewhere, the 3β sulfate resides in a separate, distinct pocket of positive charge (P-site 2) at the interface of TM6 and TM9. Within P-site 2, R362 and Q849 form electrostatic interactions with one of the sulfate's three nonbridging oxygens. A second oxygen is coordinated by Q845 and makes a water-mediated interaction with D842, creating a network of interactions that links the sulfo group to W995. The third oxygen does not form direct protein interactions but instead faces a narrow solvent-filled tunnel that continues in the direction of the extracellular face. Neither $PGE_1$ nor $PGE_2$ make notable contacts with the sidechains comprising P-site 2.

Although the two helical bundles clamp around the substrates in all three structures, there is little change to the rotamers of most substrate-binding residues compared to the apo structures. The few residues that adopt new conformations include F156 and F324, which flip to line the periphery of the hydrophobic patch. The repositioning

**Table 1 | Cryo-EM data collection, refinement and validation statistics**

| | $\text{Apo}_{\text{wide}}$ MRP4<br>(EMD-40829)<br>(PDB 8SXA) | $\text{Apo}_{\text{narrow}}$ MRP4<br>(EMD-40828)<br>(PDB 8SX9) | MRP4+DHEA-S<br>(EMD-40826)<br>(PDB 8SX7) | MRP4+PGE$_1$<br>(EMD-40827)<br>(PDB 8SX8) | MRP4+PGE$_2$<br>(EMD-40830)<br>(PDB 8SXB) | MRP4+ATP-Mg$^{2+}$<br>(EMD-40821)<br>(PDB 8SWN) |
|---|---|---|---|---|---|---|
| **Data collection and processing** | | | | | | |
| Magnification | ×105,000 | ×105,000 | ×105,000 | ×105,000 | ×105,000 | ×105,000 |
| Voltage (kV) | 300 | 300 | 300 | 300 | 300 | 300 |
| Electron exposure (e$^-$/Å$^2$) | 67 | 67 | 67 | 67 | 67 | 67 |
| Exposure time (s) | 5.9 | 5.9 | 5.9 | 5.9 | 5.9 | 5.9 |
| Defocus range (μm) | −1.0 to −2.0 | −1.0 to −2.0 | −0.5 to −2.0 | −0.5 to −2.0 | −0.5 to −2.0 | −0.5 to −2.0 |
| Pixel size (Å) | 0.4175 | 0.4175 | 0.4175 | 0.4175 | 0.4175 | 0.4175 |
| Symmetry imposed | *C1* | *C1* | *C1* | *C1* | *C1* | *C1* |
| Initial particle images (no.) | 4,613,782 | 4,613,782 | 5,330,431 | 7,912,699 | 3,910,205 | 840,205 |
| Final particle images (no.) | 82,936 | 80,063 | 360,511 | 122,978 | 187,047 | 104,051 |
| Map resolution (Å) | 3.3 | 3.3 | 2.7 | 3.5 | 2.9 | 3.1 |
| FSC threshold | 0.143 | 0.143 | 0.143 | 0.143 | 0.143 | 0.143 |
| Map resolution range (Å) | 30–3.3 | 30–3.3 | 30–2.7 | 30–3.5 | 30–2.9 | 30–3.1 |
| **Refinement** | | | | | | |
| Initial model used (PDB code) | 6BHU | 6BHU | 8SXA | 8SXA | 8SXA | 8SXA |
| Model resolution (Å) | | | | | | |
| Masked | 3.5 | 3.5 | 2.9 | 3.6 | 3.1 | 3.2 |
| Fourier shell correlation (FSC) threshold | 0.5 | 0.5 | 0.5 | 0.5 | 0.5 | 0.5 |
| Map resolution range (Å) | 30–3.5 | 30–3.5 | 30–2.9 | 30–3.6 | 30–3.1 | 30–3.2 |
| Map sharpening *B* factor (Å$^2$) | −121.4 | −137.4 | −97.6 | −121.5 | −106.9 | −106.5 |
| Model composition | | | | | | |
| Nonhydrogen atoms | 9,178 | 9,178 | 9,521 | 9,418 | 9,202 | 9,155 |
| Protein residues | 1,153 | 1,153 | 1,188 | 1,175 | 1,152 | 1,135 |
| Water | 0 | 0 | 3 | 1 | 1 | 0 |
| Ligands | 0 | 0 | ZWY: 1 | XPG: 1 | P2E: 1 | MG: 2 ATP: 2 PTY: 1 |
| *B* factors (Å$^2$) minimum/maximum/mean | | | | | | |
| Protein | 29.93/215.93/118.88 | 43.67/236.79/136.47 | 1.73/190.69/85.26 | 34.87/204.17/100.34 | 7.57/190.27/89.80 | 94.85/279.65/143.82 |
| Ligand | – | – | 10.47/41.83/24.62 | 46.19/46.19/46.19 | 37.95/55.85/44.75 | 128.82/181.22/148.41 |
| Root mean square deviations | | | | | | |
| Bond lengths (Å) (greater than 4σ) | 0.006 (0) | 0.006 (0) | 0.004 (0) | 0.005 (0) | 0.006 (1) | 0.0056 (0) |
| Bond angles (°) (greater than σ) | 0.675 (0) | 0.681 (0) | 0.674 (0) | 0.831 (0) | 0.898 (3) | 0.686 (2) |
| **Validation** | | | | | | |
| MolProbity score | 1.18 | 1.01 | 1.12 | 0.78 | 0.77 | 0.77 |
| Clashscore | 2.96 | 2.31 | 2.34 | 0.94 | 0.64 | 0.86 |
| Poor rotamers (%) | 0 | 0 | 0 | 0 | 0 | 0 |
| Ramachandran plot | | | | | | |
| Favored (%) | 97.55 | 98.08 | 97.46 | 98.03 | 97.73 | 98.76 |
| Allowed (%) | 2.45 | 1.92 | 2.54 | 1.97 | 2.27 | 1.24 |
| Outliers (%) | 0 | 0 | 0 | 0 | 0 | 0 |

of F156 enables R946 to rotate from facing out of the helical bundle (in the direction of the lasso motif) to facing in toward the central cavity, where its guanidino group contributes to P-site 1. A similar inward rotation by H153 adds further positive-charge character to the pocket relative to either apo structure (Fig. 5b).

In the ATP-bound state, the transmembrane regions of MRP4 are in an arrangement incompatible with substrate binding. The two halves of the transporter have rotated inward toward the central cavity, and F211, L367 and F368 from the hydrophobic patch are within van der Waals contact distance of W995, sterically preventing DHEA-S

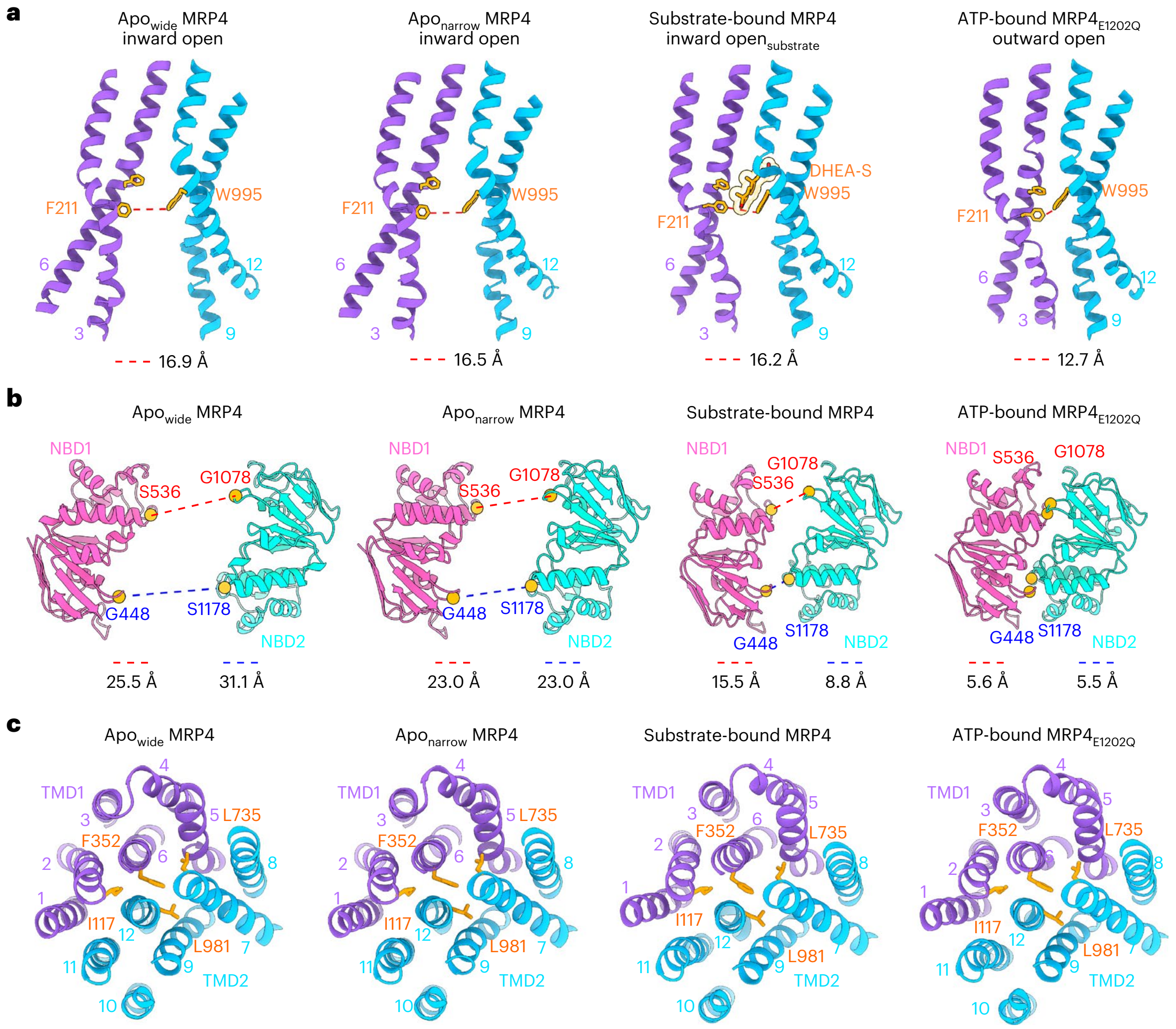

**Fig. 3 | Comparison of the inward-open, inward-narrow and outward-occluded conformations of MRP4. a**, Side view of the TMDs from the plane of the membrane for apo-, substrate-bound (DHEA-S-bound structure shown) and ATP-bound states. Select substrate-binding residues from either TMD are shown with a stick representation. The distance between the C$_\alpha$ atoms of two substrate-binding residues, F211 and W995, is drawn as a red dashed line, with measured values indicated. **b**, Bottom view of the NBDs, seen from the direction of the cytoplasm. C$_\alpha$ of signature sequence serine and Walker A glycine shown as orange spheres. Distances between opposing pairs of residues at either NBS are shown as dashed lines; blue for NBS1 and red for NBS2. Distance values are indicted. **c**, Top-down views of the extracellular face. Residues of the extracellular gate (I117, F352, L735 and L981) are shown with a stick representation and colored orange. Domains follow the color scheme presented in Fig. 1a.

or either prostaglandin from occupying the site (Fig. 5f). ATP binding also results in the intrusion of TMD2 hydrophobic residues into the regions of positive charge at either end of the substrate-binding pocket. P-site 1 is disrupted by the insertion of F156 and H152, displacing the substrate-binding residues Q994 and R998. Q994 rotates away to neutralize D953 from TM11, while R998 adopts electrostatic interactions with Q160 and Q999 and forms a salt bridge with E1002 (Fig. 5g). In P-site 2, F324 occupies the former site of the DHEA-S sulfo group (Fig. 5h). Of the residues previously involved in coordinating the sulfate, R362 and N849 hydrogen bond with one another, while N845 flips away and is stabilized by the backbone carbonyl of L321. The tight packing observed at both P-sites and between the hydrophobic patch and W995 from TMD2 is consistent with substrate expulsion from the binding site, although no clear exit pathway is observed in our structure.

## Structural comparison of MRP4 and MRP1

MRP4 shares 37% sequence identity with MRP1 (Extended Data Fig. 1). While both are recognized as transporters of amphipathic organic anions, only MRP1 is well-established as a transporter of glutathione conjugates, including the eicosanoid LTC$_4$. In our studies, LTC$_4$ failed to stimulate MRP4, unlike reported effects on MRP1 (ref. 47). Differences in the binding sites of substrate-bound MRP4 and MRP1 are consistent with their respective substrate specificities. Superimposing the structure of DHEA-S-bound MRP4 onto LTC$_4$-bound MRP1 (Protein Data Bank (PDB) ID 5UJA), aligned via the second transmembrane bundle, shows that the MRP4 substrate-binding site is narrower and lacks shape complementarity to the leukotriene (Fig. 6a). Transmembrane bundle 1 of MRP4 is rotated by roughly 13° toward the central axis of the transporter compared to its position in MRP1, resulting in an apparent clash between the glutathione moiety of LTC$_4$ and the observed conformations of MRP4 TM2 residues (Fig. 6b).

Of the 15 MRP1 residues involved in LTC$_4$ binding, ten are identical or similar at the equivalent positions in MRP4, while the remaining five are altered (Fig. 6c). Two MRP1 residues (K332 and H335) that hydrogen bond with a carboxyl from the LTC$_4$ glutathione moiety are replaced by a T99 and E102 in MRP4, forming an acidic pocket in place of the basic one in MRP1 (Fig. 6d). M1092 in MRP1, part of the hydrophobic portion

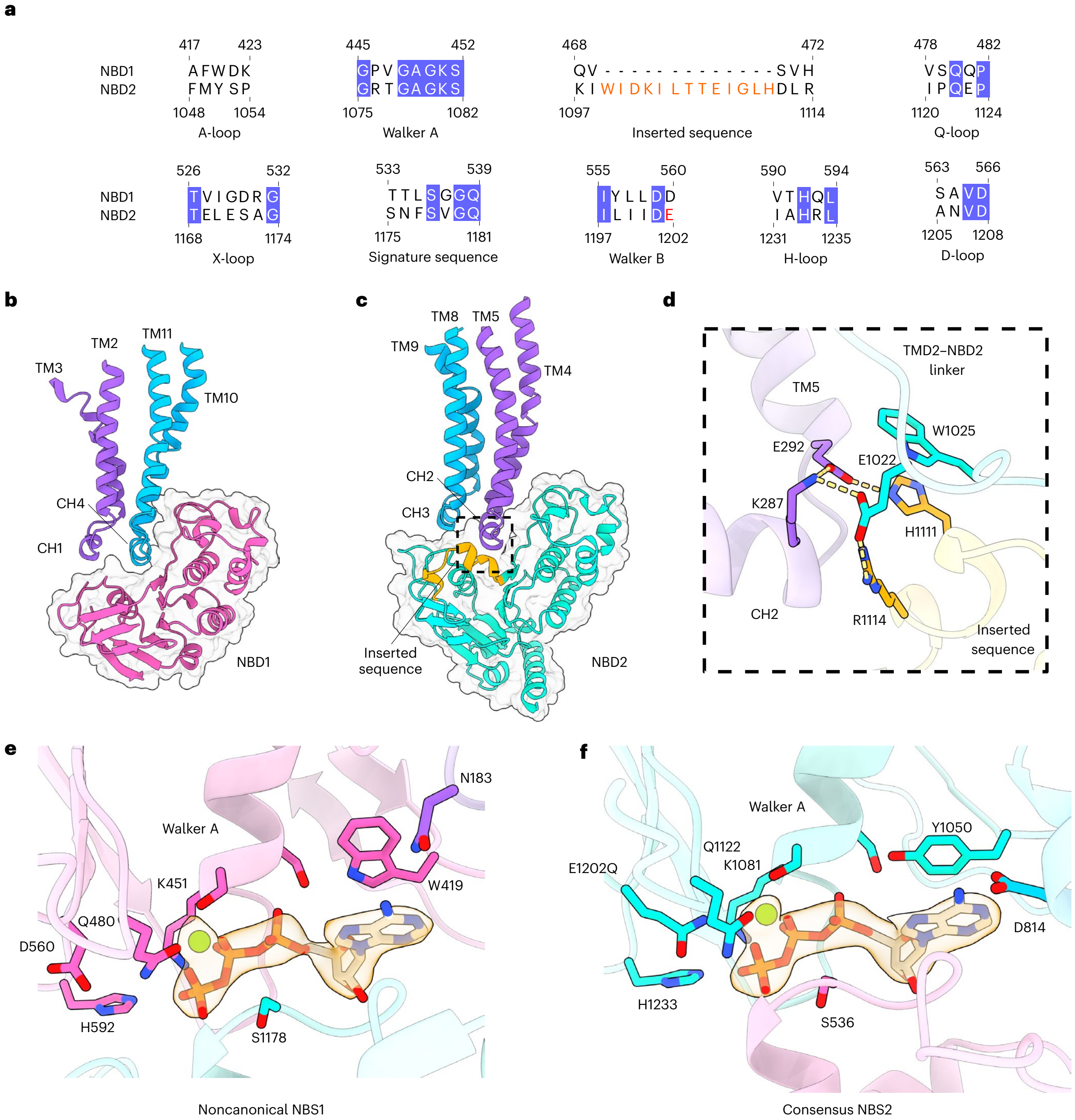

**Fig. 4 | Structural asymmetry between NBD1 and NBD2. a**, Sequence alignment of selected motifs from NBD1 and NBD2. Conserved residues are highlighted in blue, residues of the inserted sequence are orange and the position of E1202Q mutant in NBD2 Walker B is in red. **b**,**c**, Side view of the TMD interactions with NBD1 (**b**) and NBD2 (**c**) in the ATP-bound MRP4$_{E1202Q}$ structure. Ribbon diagram of domains are colored as in Fig. 1a, and are overlaid on a surface of either NBD in transparent gray. The inserted sequence in NBD2 is highlighted in orange. **d**, Enlarged view of the box in **c**. Electrostatic interactions between the inserted sequence, CH2, and the TMD2-NBD2 linker, with residues shown as sticks. Hydrogen bonds and salt bridges are indicated by yellow dashed lines. **e**,**f**, Close-up views of the noncanonical NBS1 (**e**) and NBS2 (**f**) featuring the mutated catalytic residue in the ATP-bound MRP4$_{E1202Q}$ structure. Selected side chains from interacting motifs are shown as sticks. ATP is shown as sticks, $Mg^{2+}$ as green spheres and densities for both are shown as a transparent surface. For clarity, only the ATP-$Mg^{2+}$ density is shown.

of the binding site that packs against the lipid tail of $LTC_4$, is equivalent to D842 in MRP4, which has a crucial role in orienting the polar groups of DHEA-S and the prostaglandins. T550 in MRP1 is replaced by L321 in MRP4, which could sterically hinder $LTC_4$ from binding the site. Although alignment of MRP4 and MRP1 reveals differences at critical residues involved in substrate binding, the extent to which these differences account for MRP4's lack of specificity for glutathione conjugates remains to be determined.

The ATP-bound MRP4$_{E1202Q}$ structure reveals a state along the MRP subfamily transport cycle that differs substantially from that

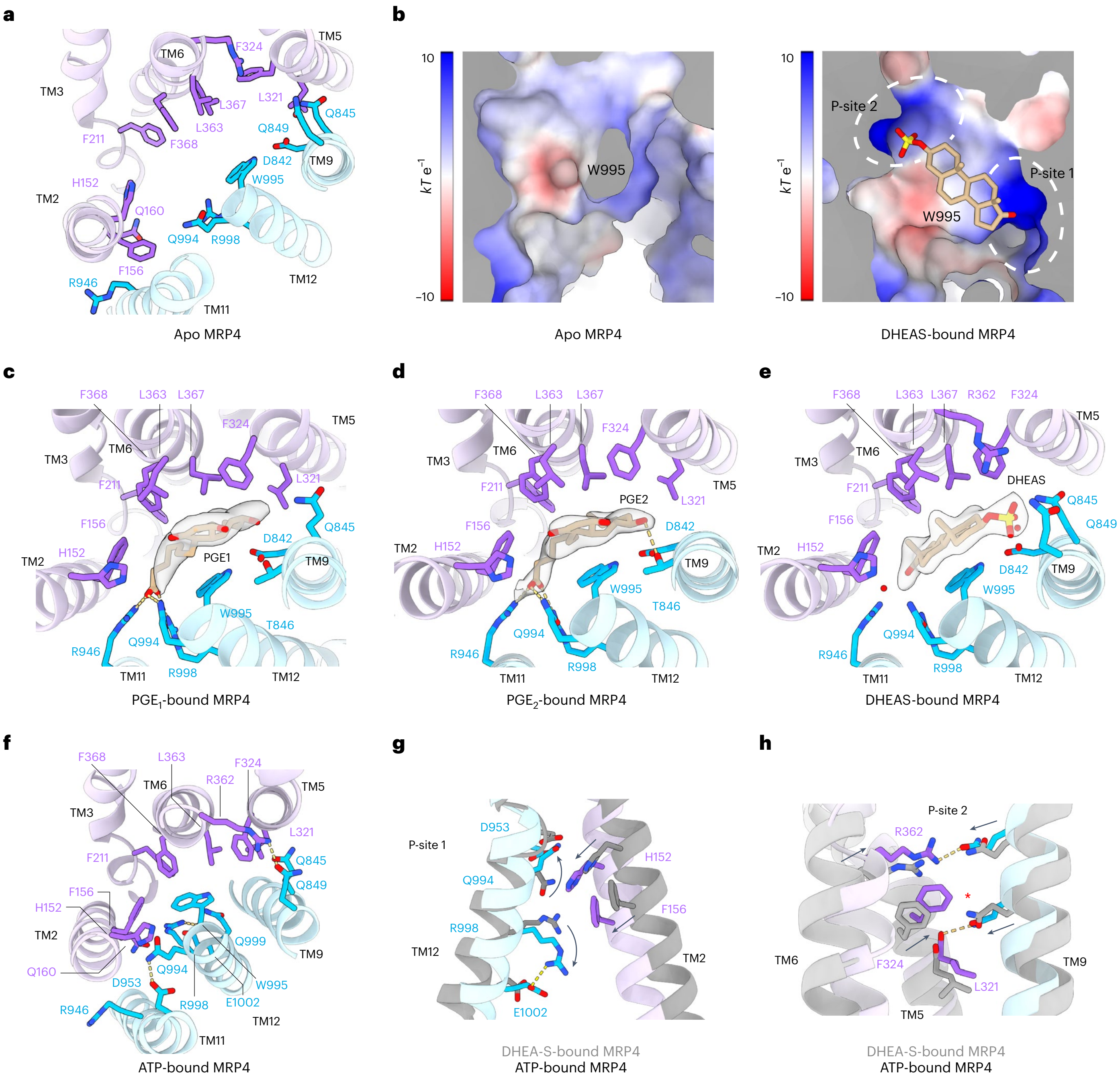

Apo MRP4

Apo MRP4

DHEAS-bound MRP4

PGE$_1$-bound MRP4

PGE$_2$-bound MRP4

DHEAS-bound MRP4

ATP-bound MRP4

DHEA-S-bound MRP4
ATP-bound MRP4

DHEA-S-bound MRP4
ATP-bound MRP4

**Fig. 5 | DHEA-S and prostaglandin binding to MRP4. a–f**, Top-down view of the substrate-binding pocket (**a**), the apo$_{\mathrm{wide}}$, inward-open$_{\mathrm{substrate}}$ state (**b**), the inward-open$_{\mathrm{substrate}}$ state bound to PGE$_1$ (**c**), the inward-open$_{\mathrm{substrate}}$ state bound to PGE$_2$ (**d**), the inward-open$_{\mathrm{substrate}}$ state bound to DHEA-S (**e**) and the outward-occluded state of MRP4$_{\mathrm{E1202Q}}$ bound to ATP-Mg$^{2+}$ (**f**). Residues shown form van der Waals contacts, hydrogen bonds or salt bridges with any of the three substrates. Substrates are represented by sticks. For clarity, only substrate densities are shown as transparent surfaces. Waters are depicted as red spheres, and electrostatic interactions are indicated as yellow dashed lines. **b**, Electrostatic potentials (shown as a scale ranging from −10 $kT e^{-1}$ in red to 10 $kT e^{-1}$ in blue) of the substrate-binding surfaces of the MRP4 TMD2 in the apo$_{\mathrm{wide}}$, inward-open state (left) and the inward-open$_{\mathrm{substrate}}$, DHEA-S-bound state (right). Dashed circles highlight P-sites 1 and 2 that assemble on substrate binding. **g**,**h**, Local conformational changes at P-site 1 (**g**) and P-site 2 (**h**) as MRP4 transitions from the inward-open$_{\mathrm{substrate}}$ state to the outward-occluded, ATP-Mg$^{2+}$-bound state. The DHEA-S-bound structure is shown in gray and the ATP-bound structure is colored as in Fig. 1a. Black arrows indicate movement of sidechains. Electrostatic interactions are shown as yellow dashed lines. Red asterisks indicate positions of substrate polar groups in their respective structures (an unoccupied P-site 2 and the C1 carboxyl in P-site 1 in the PGE$_1$ and PGE$_2$ bound structures; the 3β sulfate in P-site 2 and a coordinated water in P-site 1 in the DHEA-S bound structure).

of ATP-bound MRP1 (PDB ID 6BHU) (Fig. 6e). While MRP1 assumes an outward-open conformation on ATP binding that features a narrow channel between helices 6, 11, 12 and 17 extending from the substrate-binding residues to the extracellular milieu, ATP-bound MRP4$_{\mathrm{E1202Q}}$ contains a closed extracellular gate with no apparent substrate exit tunnel. The closure of this extracellular pathway is independent of ATP hydrolysis or subsequent phosphate release, consistent with an alternating-access mechanism for directionality of substrate transport where the extracellular face resets before the cytoplasmic portions of the transporter.

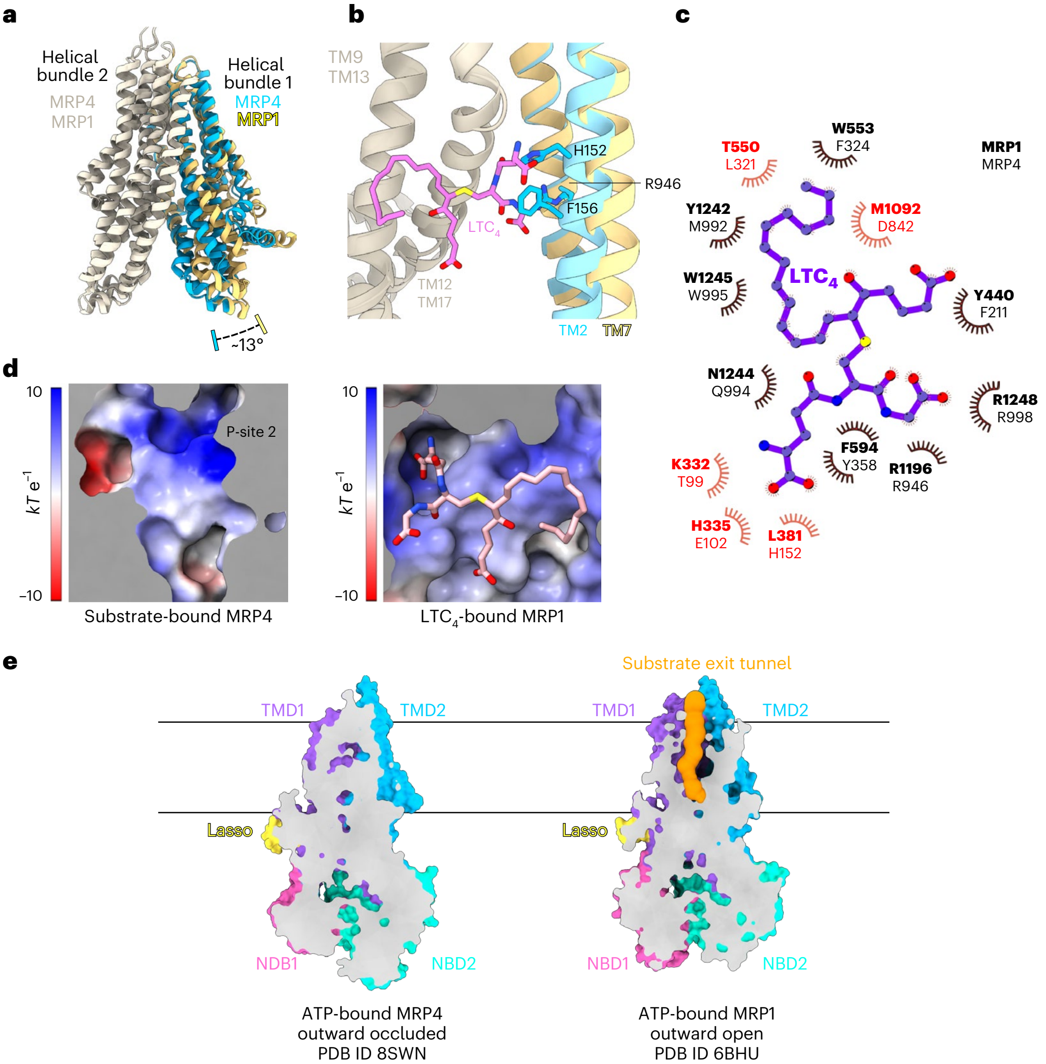

**Fig. 6 | Structural comparison between MRP4 and related ABCC family members. a**, TMDs of MRP1 and MRP4 aligned through helical bundle 2. Helical bundle 2 is colored bone for both transporters. Helical bundle 1 is colored canary in MRP1 and cyan in MRP4. The relative angle of rotation between helical bundle 1 of MRP1 and MRP4 with respect to helical bundle 2 is indicated. **b**, Close-up view of the superimposed structures of $LTC_4$-bound MRP1 and DHEA-S-bound MRP4 (DHEA-S not shown for clarity). $LTC_4$ sterically clashes against H152, F156 and R946 as a result of the narrower substrate-bound conformation of MRP4. Transmembrane regions colored as in **a**, $LTC_4$ and the side chains of MRP4 shown as sticks. **c**, Schematic of MRP1 bound to $LTC_4$ (PDB 5UJA). MRP1 residues involved in ligand binding are in bold, and aligned MRP4 residues are non-bold. Red text signified a change in polarity between MRP1 and corresponding MRP4 residues. **d**, Electrostatic potentials (shown as a scale ranging from −10 $kT\,e^{-1}$ in red to 10 $kT\,e^{-1}$ in blue) of the aligned substrate-binding surfaces of TMD2 of MRP4 bound to DHEA-S (not shown for clarity) and TMD2 of MRP1 bound to $LTC_4$. An acidic patch in MRP4 replaces a basic surface for coordinating glutathione carboxyl groups. $LTC_4$ shown as sticks, colored magenta and by heteroatom. **e**, Slice-through of ATP-bound MRP4 and ATP-bound MRP1, reveals a substrate exit tunnel present only in the MRP1 structure, while MRP4 is outward-facing occluded. Transmembrane regions of MRP4 and aligned regions of MRP1 are colored as in Fig. 1. TMD0 of MRP1 hidden for clarity. The volume of the MRP1 substrate exit tunnel is shown as an orange surface.

## Discussion

Based on our structures and that of the closely related ATP-bound $MRP1_{E1454Q}$, we propose a model for MRP4 substrate transport (Fig. 7a). Under substrate- and nucleotide-free conditions, MRP4 fluctuates along a landscape of inward-open states that vary in the angle between the two halves of the transporter. An amphipathic substrate-binding site, comprising a hydrophobic region on TMD1 and two distinct positively charged pockets, is located between the two helical bundles and recognizes a variety of organic anions. Substrate binding brings the two helical bundles toward each other and shortens the inter-NBD distance, priming them for an accelerated rate of dimerization in the presence of ATP-$Mg^{2+}$.

Nucleotide binding drives the conformational transition that results in substrate transport. Our ATP-bound $MRP4_{E1202Q}$ structure shows dimerized NBDs and no observable exit pathway connecting substrate-binding residues to the extracellular space. Following the alternating-access model proposed for MRP1 and other ABC transporters, our ATP-bound structure represents a state after substrate translocation, where the extracellular gate has closed but ATP hydrolysis and phosphate release have not yet reset the cytoplasmic portions of the transporter. Although $PGE_2$ was added to our sample to stimulate NBD dimerization and capture a larger portion of $MRP4_{E1202Q}$ in an ATP-bound state, we expect a substrate is not necessary for MRP4 to adopt this outward-occluded conformation.

Our structure of outward-occluded MRP4 stands in contrast to that of ATP-bound MRP1, where cryo-EM analysis of the analogous Walker A mutant $MRP1_{E1454Q}$ under similar conditions exclusively resolved an outward-open transporter. Extensive processing of our $MRP4_{E1202Q}$ dataset provided no evidence for an outward-open conformation, although we found several two-dimensional classes matching our

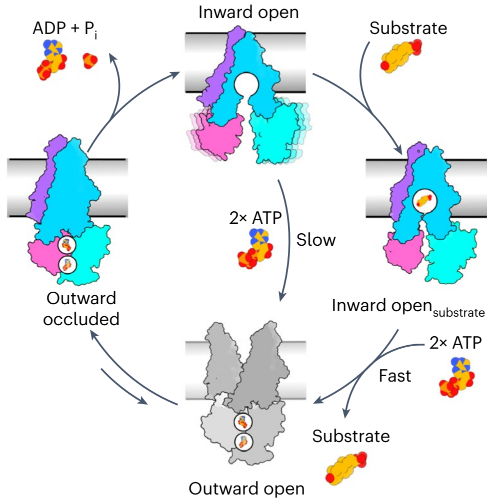

**Fig. 7 | Proposed translocation cycle of MRP4.** Cartoon representation of the alternate access transport mechanism of MRP4. The inward-open, inward-open$_{\text{substrate}}$ and outward-occluded states are derived from the cryo-EM structures in this study, while the putative outward-open state is based on the structure of ATP-bound MRP1 (PDB ID 6BHU). The cycle begins with MRP4 open toward the cytoplasm, featuring a solvent-accessible substrate-binding cavity and widely separated NBDs. The distance between the NBDs varies due to thermal fluctuations. When bound to substrate, the two halves of MRP4 constrict toward one another, reducing the volume of the central cavity and bringing the NBDs into close proximity. ATP binding dimerizes the NBDs and induces substrate transport by allosterically deforming the substrate-binding site and opening an exit pathway for substrate release. Inward-open MRP4 is capable of binding ATP in the absence of substrate and proceeding to this speculated outward-open conformation, although at a notably slower rate due to the increased distance between NBDs. In the outward-occluded state, the transmembrane helices lining the exit pathway have reset, leaving the substrate-binding site exposed to neither the cytoplasm nor extracellular space. Progression to the outward-occluded state occurs regardless of substrate presence. ATP hydrolysis and subsequent nucleotide and $P_i$ release allows for dissociation of the NBD dimer and return to the inward-open state. Cartoon domains follow the color scheme presented in Fig. 1a.

apo$_{\text{wide}}$ structure (Supplementary Fig. 6). These results indicate MRP4's outward-open conformation might be more transient than that of MRP1, reflecting differences in their energy landscapes. Without an outward-open structure, the nature of substrate release by MRP4 remains unclear. It is uncertain whether this putative conformation would have an exit tunnel like MRP1, or if the substrate-binding site might instead open toward the lipid environment.

Outward-occluded states have been reported for various bacterial exporters, including MsbA[48], TmrAB[49], Cgt[50] and McjD[51], as well as the eukaryotic phosphatidylcholine exporter ABCB4[52]. Although the topologies for each transporter differ, these structures are thought to represent similar states in the above model of substrate transport. ATP-bound MRP4$_{\text{E1202Q}}$ most strongly resembles the structure of the ADP or ATP-bound SUR1, an ABCC family member that acts as the ADP sensor of the KATP channel[53] (Extended Data Fig. 5). Despite SUR1 sequence homology to the MRP subfamily and overall structural resemblance to a canonical ABC transporter, it has no known transport substrates and is thought to exclusively regulate channel activity. The ATP-bound MRP4 and ADP or ATP-bound SUR1 both contain a closed extracellular gate and tightly packed TMDs sealed off from the cytoplasm, suggesting conformational similarity of MRP4 to the ABCC family extends beyond the MRPs.

Our findings suggest that unlike other reported MRP4 substrates, $PGE_1$, $PGE_2$ and DHEA-S stimulate the ATPase activity of the transporter with apparent $K_m$ values in the micromolar range. The inward-open$_{\text{substrate}}$ state of MRP4 contains two positively charged pockets not found in apo MRP4. These pockets can accommodate anionic groups and are positioned at opposite ends of the binding site, potentially contributing to the diverse range of substrates recognized by MRP4. MRP4 buries the nonpolar cores of prostaglandins and DHEA-S between a hydrophobic region on TMD1 and W995 on TMD2, resembling the 'tryptophan-sandwich' observed in $LTC_4$-bound MRP1 (ref. 47). This suggests a common mechanism among the MRPs for sequestering hydrophobic cargo. Our substrate-bound structures align with previous MRP4 mutagenesis studies that identified critical roles for F368, W995 and R998 (refs. 54,55) in substrate transport.

Our two prostaglandin-bound structures reveal comparable interactions between MRP4 and the polar substituents of either prostaglandin. Given that these functional groups are common to other prostanoids shown to be transported by MRP4, including $PGD_2$, $PGF_{2\alpha}$ and $TXB_2$ (refs. 17,19,20), it is likely that these ligands bind through similar contacts. Furthermore, these chemical features are shared across many other prostaglandins, suggesting the diversity of prostaglandins and their analogs transported by MRP4 may be underappreciated.

The result that prostaglandin and DHEA-S stimulate MRP4 ATPase activity contrasts with the remaining substrates tested, including the cyclic nucleotides. Despite reports that identify MRP4 as a cyclic nucleotide transporter[24,56,57], high concentrations of cAMP and cGMP did not notably stimulate MRP4 ATPase activity in vitro. Our cryo-EM results failed to confirm a high-affinity complex between cAMP and MRP4, with the final reconstruction lacking both an observed density for cAMP and any notable conformational change compared to the inward-open apo states. While we cannot rule out cAMP as an MRP4 substrate, these results indicate that any transport of cyclic nucleotides in our reconstituted system occurs at or below the basal activity of MRP4, and that cAMP binding does not induce an inward-open$_{\text{substrate}}$ state. Downstream signaling of various prostaglandins through their respective G-protein-coupled receptors affects the levels of cytoplasmic cAMP[58], providing one possible mechanism for regulation of this cyclic nucleotide by MRP4. Further investigations will be necessary to clarify the precise molecular details of transport of cAMP and other nonstimulating substrates by MRP4.

Our study presents atomic-level descriptions of MRP4 in multiple conformations, revealing the basis of its organic anion specificity. The structures of $PGE_1$ and $PGE_2$ bound to MRP4 underscore the role of this transporter in prostaglandin efflux, a signaling mechanism central to numerous physiological processes. The outward-occluded structure fills in a previously unobserved but assumed state of the MRP translocation cycle and can be used as the basis for homology models of other MRPs. Our series of apo and substrate-bound inward-facing structures will provide the groundwork for computational studies aimed at validating endogenous and xenobiotic substrates of MRP4 and will aid in structure-guided designs of inhibitors for this promiscuous transporter. Improved understanding of MRP4 function will aid in addressing multidrug resistance and transporter dysregulation.

## Online content

Any methods, additional references, Nature Portfolio reporting summaries, source data, extended data, supplementary information, acknowledgements, peer review information; details of author contributions and competing interests; and statements of data and code availability are available at https://doi.org/10.1038/s41594-023-01176-4.

## References

1. Chabowski, D. S., Cohen, K. E., Abu-Hatoum, O., Gutterman, D. D. & Freed, J. K. Crossing signals: bioactive lipids in the microvasculature. *Am. J. Physiol. Heart Circ. Physiol.* **318**, H1185–H1197 (2020).
2. Harizi, H. & Gualde, N. The impact of eicosanoids on the crosstalk between innate and adaptive immunity: the key roles of dendritic cells. *Tissue Antigens* **65**, 507–514 (2005).

3. Martens, M. D., Fernando, A. S. & Gordon, J. W. A new trick for an old dog? Myocardial-specific roles for prostaglandins as mediators of ischemic injury and repair. *Am. J. Physiol. Heart Circ. Physiol.* **320**, H2169–H2184 (2021).
4. Mitchell, J. A. & Kirkby, N. S. Eicosanoids, prostacyclin and cyclooxygenase in the cardiovascular system. *Br. J. Pharmacol.* **176**, 1038–1050 (2019).
5. Oyesola, O. O. & Tait Wojno, E. D. Prostaglandin regulation of type 2 inflammation: from basic biology to therapeutic interventions. *Eur. J. Immunol.* **51**, 2399–2416 (2021).
6. Vannuccini, S., Bocchi, C., Severi, F. M., Challis, J. R. & Petraglia, F. Endocrinology of human parturition. *Ann. Endocrinol.* **77**, 105–113 (2016).
7. Zeilhofer, H. U. Prostanoids in nociception and pain. *Biochem. Pharmacol.* **73**, 165–174 (2007).
8. Biringer, R. G. The enzymology of the human prostanoid pathway. *Mol. Biol. Rep.* **47**, 4569–4586 (2020).
9. Johnson, A. M., Kleczko, E. K. & Nemenoff, R. A. Eicosanoids in cancer: new roles in immunoregulation. *Front Pharm.* **11**, 595498 (2020).
10. Mitchell, J. A. et al. Cyclooxygenases and the cardiovascular system. *Pharmacol. Ther.* **217**, 107624 (2021).
11. Wang, D., Cabalag, C. S., Clemons, N. J. & DuBois, R. N. Cyclooxygenases and prostaglandins in tumor immunology and microenvironment of gastrointestinal cancer. *Gastroenterology* **161**, 1813–1829 (2021).
12. Beaman, J., Prifti, C., Schwarz, E. B. & Sobota, M. Medication to manage abortion and miscarriage. *J. Gen. Intern Med* **35**, 2398–2405 (2020).
13. Klimko, P. G. & Sharif, N. A. Discovery, characterization and clinical utility of prostaglandin agonists for the treatment of glaucoma. *Br. J. Pharmacol.* **176**, 1051–1058 (2019).
14. Lang, I. M. & Gaine, S. P. Recent advances in targeting the prostacyclin pathway in pulmonary arterial hypertension. *Eur. Respir. Rev.* **24**, 630–641 (2015).
15. Lee, O. Y. et al. A comparative study of DA-9601 and misoprostol for prevention of NSAID-associated gastroduodenal injury in patients undergoing chronic NSAID treatment. *Arch. Pharm. Res* **37**, 1308–1316 (2014).
16. Stephenson, M. L. & Wing, D. A. Misoprostol for induction of labor. *Semin Perinatol.* **39**, 459–462 (2015).
17. Reid, G. et al. The human multidrug resistance protein MRP4 functions as a prostaglandin efflux transporter and is inhibited by nonsteroidal antiinflammatory drugs. *Proc. Natl Acad. Sci. USA* **100**, 9244–9249 (2003).
18. Wen, J. et al. The pharmacological and physiological role of multidrug-resistant protein 4. *J. Pharmacol. Exp. Ther.* **354**, 358–375 (2015).
19. Rius, M., Thon, W. F., Keppler, D. & Nies, A. T. Prostanoid transport by multidrug resistance protein 4 (MRP4/ABCC4) localized in tissues of the human urogenital tract. *J. Urol.* **174**, 2409–2414 (2005).
20. Tanaka, N., Kawai, J., Hirasawa, N., Mano, N. & Yamaguchi, H. ATP-Binding cassette transporter C4 is a prostaglandin D2 exporter in HMC-1 cells. *Prostaglandins Leukot. Ess. Fat. Acids* **159**, 102139 (2020).
21. Kalinski, P. Regulation of immune responses by prostaglandin $E_2$. *J. Immunol.* **188**, 21–28 (2012).
22. Kochel, T. J., Reader, J. C., Ma, X., Kundu, N. & Fulton, A. M. Multiple drug resistance-associated protein (MRP4) exports prostaglandin $E_2$ ($PGE_2$) and contributes to metastasis in basal/triple negative breast cancer. *Oncotarget* **8**, 6540–6554 (2017).
23. Zelcer, N. et al. Steroid and bile acid conjugates are substrates of human multidrug-resistance protein (MRP) 4 (ATP-binding cassette C4). *Biochem. J.* **371**, 361–367 (2003).
24. Chen, Z. S., Lee, K. & Kruh, G. D. Transport of cyclic nucleotides and estradiol 17-b-D-glucuronide by multidrug resistance protein 4. Resistance to 6-mercaptopurine and 6-thioguanine. *J. Biol. Chem.* **276**, 33747–33754 (2001).
25. Hara, Y. et al. Inhibition of MRP4 prevents and reverses pulmonary hypertension in mice. *J. Clin. Invest.* **121**, 2888–2897 (2011).
26. Decouture, B. et al. Impaired platelet activation and cAMP homeostasis in MRP4-deficient mice. *Blood* **126**, 1823–1830 (2015).
27. Li, C. et al. Spatiotemporal coupling of cAMP transporter to CFTR chloride channel function in the gut epithelia. *Cell* **131**, 940–951 (2007).
28. Moon, C. et al. Compartmentalized accumulation of cAMP near complexes of multidrug resistance protein 4 (MRP4) and cystic fibrosis transmembrane conductance regulator (CFTR) contributes to drug-induced diarrhea. *J. Biol. Chem.* **290**, 11246–11257 (2015).
29. Chen, Z. S. et al. Analysis of methotrexate and folate transport by multidrug resistance protein 4 (ABCC4): MRP4 is a component of the methotrexate efflux system. *Cancer Res.* **62**, 3144–3150 (2002).
30. Ci, L. et al. Involvement of MRP4 (ABCC4) in the luminal efflux of ceftizoxime and cefazolin in the kidney. *Mol. Pharmacol.* **71**, 1591–1597 (2007).
31. Imaoka, T. et al. Functional involvement of multidrug resistance-associated protein 4 (MRP4/ABCC4) in the renal elimination of the antiviral drugs adefovir and tenofovir. *Mol. Pharmacol.* **71**, 619–627 (2007).
32. Kohler, J. J. et al. Tenofovir renal proximal tubular toxicity is regulated by OAT1 and MRP4 transporters. *Lab. Invest.* **91**, 852–858 (2011).
33. Ray, A. S. et al. Mechanism of active renal tubular efflux of tenofovir. *Antimicrob. Agents Chemother.* **50**, 3297–3304 (2006).
34. Rius, M., Hummel-Eisenbeiss, J., Hofmann, A. F. & Keppler, D. Substrate specificity of human ABCC4 (MRP4)-mediated cotransport of bile acids and reduced glutathione. *Am. J. Physiol. Gastrointest. Liver Physiol.* **290**, G640–G649 (2006).
35. Rius, M., Hummel-Eisenbeiss, J. & Keppler, D. ATP-dependent transport of leukotrienes B4 and C4 by the multidrug resistance protein ABCC4 (MRP4). *J. Pharmacol. Exp. Ther.* **324**, 86–94 (2008).
36. Rius, M., Nies, A. T., Hummel-Eisenbeiss, J., Jedlitschky, G. & Keppler, D. Cotransport of reduced glutathione with bile salts by MRP4 (ABCC4) localized to the basolateral hepatocyte membrane. *Hepatology* **38**, 374–384 (2003).
37. Vogt, K. et al. Release of platelet-derived sphingosine-1-phosphate involves multidrug resistance protein 4 (MRP4/ABCC4) and Is inhibited by statins. *Thromb. Haemost.* **118**, 132–142 (2018).
38. Hagmann, W. et al. Purification of the human apical conjugate export pump MRP2 reconstitution and functional characterization as substrate-stimulated ATPase. *Eur. J. Biochem.* **265**, 281–289 (1999).
39. Mao, Q., Leslie, E. M., Deeley, R. G. & Cole, S. P. ATPase activity of purified and reconstituted multidrug resistance protein MRP1 from drug-selected H69AR cells. *Biochim. Biophys. Acta* **1461**, 69–82 (1999).
40. Shapiro, A. B. & Ling, V. ATPase activity of purified and reconstituted P-glycoprotein from Chinese hamster ovary cells. *J. Biol. Chem.* **269**, 3745–3754 (1994).
41. Sauna, Z. E., Nandigama, K. & Ambudkar, S. V. Multidrug resistance protein 4 (ABCC4)-mediated ATP hydrolysis: effect of transport substrates and characterization of the post-hydrolysis transition state. *J. Biol. Chem.* **279**, 48855–48864 (2004).
42. Berthier, J., Arnion, H., Saint-Marcoux, F. & Picard, N. Multidrug resistance-associated protein 4 in pharmacology: overview of its contribution to pharmacokinetics, pharmacodynamics and pharmacogenetics. *Life Sci.* **231**, 116540 (2019).

43. Stockner, T., Gradisch, R. & Schmitt, L. The role of the degenerate nucleotide binding site in type I ABC exporters. *FEBS Lett.* **594**, 3815–3838 (2020).
44. Copsel, S. et al. Multidrug resistance protein 4 (MRP4/ABCC4) regulates cAMP cellular levels and controls human leukemia cell proliferation and differentiation. *J. Biol. Chem.* **286**, 6979–6988 (2011).
45. Hayashi, H. et al. Sorting nexin 27 interacts with multidrug resistance-associated protein 4 (MRP4) and mediates internalization of MRP4. *J. Biol. Chem.* **287**, 15054–15065 (2012).
46. Payen, L. F., Gao, M., Westlake, C. J., Cole, S. P. & Deeley, R. G. Role of carboxylate residues adjacent to the conserved core Walker B motifs in the catalytic cycle of multidrug resistance protein 1 (ABCC1). *J. Biol. Chem.* **278**, 38537–38547 (2003).
47. Johnson, Z. L. & Chen, J. Structural basis of substrate recognition by the multidrug resistance protein MRP1. *Cell* **168**, 1075–1085 e9 (2017).
48. Mi, W. et al. Structural basis of MsbA-mediated lipopolysaccharide transport. *Nature* **549**, 233–237 (2017).
49. Hofmann, S. et al. Conformation space of a heterodimeric ABC exporter under turnover conditions. *Nature* **571**, 580–583 (2019).
50. Sedzicki, J. et al. Mechanism of cyclic beta-glucan export by ABC transporter Cgt of Brucella. *Nat. Struct. Mol. Biol.* **29**, 1170–1177 (2022).
51. Choudhury, H. G. et al. Structure of an antibacterial peptide ATP-binding cassette transporter in a novel outward occluded state. *Proc. Natl Acad. Sci. USA* **111**, 9145–9150 (2014).
52. Olsen, J. A., Alam, A., Kowal, J., Stieger, B. & Locher, K. P. Structure of the human lipid exporter ABCB4 in a lipid environment. *Nat. Struct. Mol. Biol.* **27**, 62–70 (2020).
53. Lee, K. P. K., Chen, J. & MacKinnon, R. Molecular structure of human KATP in complex with ATP and ADP. *eLife* **6**, e32481 (2017).
54. El-Sheikh, A. A., van den Heuvel, J. J., Krieger, E., Russel, F. G. & Koenderink, J. B. Functional role of arginine 375 in transmembrane helix 6 of multidrug resistance protein 4 (MRP4/ABCC4). *Mol. Pharmacol.* **74**, 964–971 (2008).
55. Wittgen, H. G. et al. Phenylalanine 368 of multidrug resistance-associated protein 4 (MRP4/ABCC4) plays a crucial role in substrate-specific transport activity. *Biochem. Pharmacol.* **84**, 366–373 (2012).
56. Schuetz, J. D. et al. MRP4: a previously unidentified factor in resistance to nucleoside-based antiviral drugs. *Nat. Med.* **5**, 1048–1051 (1999).
57. van Aubel, R. A., Smeets, P. H., Peters, J. G., Bindels, R. J. & Russel, F. G. The MRP4/ABCC4 gene encodes a novel apical organic anion transporter in human kidney proximal tubules: putative efflux pump for urinary cAMP and cGMP. *J. Am. Soc. Nephrol.* **13**, 595–603 (2002).
58. Kawahara, K., Hohjoh, H., Inazumi, T., Tsuchiya, S. & Sugimoto, Y. Prostaglandin E2-induced inflammation: relevance of prostaglandin E receptors. *Biochim. Biophys. Acta* **1851**, 414–421 (2015).

# Methods

## MRP4 expression and membrane preparation

The wild-type bovine MRP4 gene and the $\mathrm{MRP4}_{\mathrm{E1202Q}}$ mutant were synthesized by Genscript and cloned into pFastBac with a C-terminal thrombin-cleavable 8xHis tag. For all constructs, recombinant baculovirus was produced using the Bac-to-Bac Baculovirus Expression System (Thermo Fisher Scientific). High-titer (more than $10^9$ viral particles per ml) $P_3$ virus was used to infect *Sf*9 cells at a cell density of $3 \times 10^6$ cells per ml. Cells were collected 48 h postinfection by centrifugation at 2,000*g*, flash frozen and stored at −80 °C until use. Frozen cell pellets were thawed and resuspended in lysis buffer, 50 mM Tris (pH 8.0), 300 mM NaCl, 1 mM TCEP, 1 mM phenylmethylsulfonyl fluoride (PMSF) and EDTA-free cOmplete protease inhibitor cocktail tablets (Sigma-Aldrich). The resuspended cells were repeatedly homogenized with a Dounce homogenizer, then sonicated on ice at 1 $s^{-1}$ for 5 min. Membranes were spun down at 100,000*g* for 90 min, then resuspended in working buffer (50 mM Tris (pH 8.0), 200 mM NaCl, 1 mM TCEP), supplemented with 1 mM PMSF and with EDTA-free cOmplete protease inhibitor cocktail and flash frozen in aliquots for future use.

## MRP4–nanodisc reconstitution

Thawed membranes were solubilized with 1% (w/v) *n*-dodecyl-β-D-maltopyranoside (DDM) (Anatrace) added at a detergent to protein ratio of 0.2 (w/w) and stirred for 4 h. The supernatant was separated from insoluble fractions by centrifugation at 100,000*g* for 30 min and clarified through a 0.22 µm filter. After adding 5 mM imidazole, the supernatant was batch bound to TALON IMAC resin (Clontech) for 2 h at 4 °C. The resin was washed with 10 column volumes of working buffer supplemented with 10 mM imidazole and 0.05% DDM, and then returned to working buffer supplemented with 5 mM imidazole and 0.05% DDM. Resuspended resin with bound MRP4 was mixed with Soybean Polar Lipid Extract (Avanti) to a final estimated lipid concentration of 1.2 mM and mixed for 1 h at room temperature. Purified MSP E3D1 was added to the mixture at a final concentration of 0.6 mg $ml^{-1}$ and mixed for 1 h at room temperature. Finally, 60 mg $ml^{-1}$ of methanol-activated Bio-Beads SM2 resin (Bio-Rad) was added and allowed to mix overnight at 4 °C. The heterogenous resin mixture was washed with resuspension buffer extensively to remove empty nanodiscs, and resin-bound MRP4–nanodisc complexes were eluted using buffer supplemented with 150 mM imidazole. The elution fraction was concentrated at 2,000*g* in a 100 kDa Amicon Ultra concentrator (Millipore), filtered and purified by size-exclusion chromatography (SEC) on a Superdex 200 Increase column (Cytiva) in 20 mM Tris pH 8.0, 150 mM NaCl and 1 mM TCEP. All steps were performed at 4 °C.

## ATPase assay

ATP hydrolysis by MRP4 was observed using an established NADH-coupled ATPase assay[59] by monitoring NADH fluorescence using excitation ($\lambda_{\mathrm{ex}}$) and emission ($\lambda_{\mathrm{em}}$) wavelengths of 340 nm and 445 nm, respectively, on a SpectroMax plate reader. MRP4 nanodisc (400 nM), 60 mg $ml^{-1}$ pyruvate kinase (Sigma-Aldrich), 32 mg $ml^{-1}$ lactate dehydrogenase (Sigma-Aldrich), 4 mM phosphoenolpyruvate and 150 mM NADH were mixed in 50 mM Tris pH 8.0, 150 mM KCl, 2 mM $MgCl_2$ buffer. ATP was titrated at the specified concentrations to determine the $K_m$ and $V_{\max}$ values of MRP4 ATPase activity.

We used a single, distinct preparation of MRP4 for each of the substrate titration experiments. Potential stimulation by any given putative substrate was assessed in technical triplicate. Activity measurements were normalized to the basal rate of ATPase activity in the absence of substrate within the same experiment. We evaluated basal activity for each individual preparation of MRP4 used across these assays and obtained a mean specific activity of 13.6 ± 4.5 nmol $min^{-1}$ $mg^{-1}$. ATP was held constant at 4 mM while substrate was added at the specified concentrations. All experiments assume a total molecular weight of 210 kDa for MRP4 and two copies of MSP E3D1. Data analysis was performed using GraphPad Prism, and data were fit to the Michaelis–Menten equation.

## In-gel digestion and mass spectrometry

To identify MRP4, a roughly 150 kDa gel band was excised from an SDS–PAGE gel and treated with 25 mM ammonium bicarbonate in 50% acetonitrile. Dried gel pieces were incubated with 5 mM dithiothreitol in 25 mM ammonium bicarbonate at 56 °C, followed by cooling to room temperature. Gel pieces were then incubated in 7 mM iodoacetamide in 25 mM ammonium bicarbonate at room temperature in the dark and subsequently washed with 25 mM ammonium bicarbonate in 50% acetonitrile. In-gel digestion was carried out overnight with 50 ng of trypsin in 25 mM ammonium bicarbonate. Peptides were extracted from the gel matrix with 50% acetonitrile in 0.1% formic acid, dried under vacuum and stored at −80 °C.

For LC–MS/MS analysis, an Orbitrap Fusion Lumos Tribrid mass spectrometer (Thermo Fisher Scientific) with an EASY-Spray Source (Thermo Fisher Scientific) coupled to an ACQUITY UPLC M-Class chromatography system (Waters) was used. Peptides were separated on an EASY-Spray C18 column (Thermo Fisher Scientific) using an acetonitrile gradient from 2 to 25% in 0.1% formic acid. Mass spectrometry precursor scans were recorded over a 375–1,500 $m/z$ range in the Orbitrap analyzer, and precursor peptides were selected by quadrupole isolation. Fragmentation was induced with higher-energy collisional dissociation.

For protein identification, database searches were performed against the SwissProt database totaling 551,706 entries combined with the MRP4 construct sequence. Peptide sequences were matched as tryptic peptides, allowing for one missed cleavage and carbamidomethylated cysteines as a fixed modification. Variable modifications included oxidation of methionine, N-terminal pyroglutamate from glutamine, start methionine processing and protein N-terminal acetylation. Mass accuracy tolerance was set to 20 ppm for parent and 30 ppm for fragment masses. The selected score thresholds ensured a protein false-discovery rate of less than 1%. Additional peptide mapping onto the MRP4 sequence allowed for up to two missed cleavages and one nonspecific cleavage per peptide.

## Cryo-EM sample preparation and data acquisition

Freshly purified MRP4 in lipid nanodiscs was concentrated to 0.6 mg $ml^{-1}$ for vitrification. Quantifoil R1.2/1.3 400-mesh Cu Holey Carbon Grids (EMS) were glow discharged at 15 mA for 30 s immediately before use. Sample was applied and grids were blotted using a Mark IV Vitrobot (Thermo Fisher Scientific) for 5 s at 100% humidity and 4 °C before plunge freezing in liquid $N_2$-cooled ethane. For the ATP-bound state, $\mathrm{MRP4}_{\mathrm{E1202Q}}$ in lipid nanodiscs was treated similarly, except for the addition of 1 mM $PGE_2$ and 10 mM ATP, 10 mM $MgCl_2$ followed by 10 min of incubation at 37 °C before applying on grids. The substrate-bound samples were prepared in a similar way to apo except for the inclusion of 200 µM of DHEA-S, $PGE_1$ or $PGE_2$ or 400 µM cAMP. All three substrate-bound samples were blotted on Quantifoil R1.2/1.3 300-mesh Au Holey Carbon Grids (EMS). For all samples, grids were screened for ice quality and particle density using a Talos Arctica (Thermo Fisher Scientific) microscope.

For the apo sample, 4,698 118-frame super-resolution videos were collected on an FEI Titan Krios (Thermo Fisher Scientific) operated at 300 keV, equipped with a Bioquantum energy filter (Gatan) set to a slit width of 20 eV and a post-GIF K3 camera in single-electron counting mode. The dataset was collected with a beam image-shift over a 3 × 3 hole array at a nominal magnification of ×105,000 and physical pixel size of 0.834 Å $pixel^{-1}$, using an underfocus range of 1.0 to 2.0 µm. SerialEM was used for all data acquisition using semiautomated scripts. The ATP-bound $\mathrm{MRP4}_{\mathrm{E1202Q}}$ dataset was collected on a different FEI Titan Krios using similar parameters, except for a physical pixel size of 0.835 Å $pixel^{-1}$. That dataset was composed of 3,176 super-resolution videos collected at an underfocus ranging from 0.5 to 2.0 µm.

All substrate-bound data were collected on this second FEI Titan Krios after an upgrade to Fringe-Free Imaging using a beam image-shift over a 3 × 3 hole array and recording three videos per hole. All datasets used an underfocus range of 0.5 to 2 µm. The nominal magnification and physical pixel size after upgrade were unchanged. For the DHEA-S-bound MRP4 sample, 5,609 80-frame super-resolution videos were collected. These data were merged with a dataset of 1,266 videos collected at 35° tilt, and collected using a single record per hole. Next, 7,219 80-frame super-resolution videos were collected on the $PGE_1$-bound MRP4 sample and merged with 1,034 80-frame super-resolution videos collected at 35° tilt collected using a single record per hole. Finally, 8,649 80-frame super-resolution videos were collected on the $PGE_2$-bound MRP4 sample.

### Image processing

MotionCor2 (ref. 60) was used to correct all video stacks for beam-induced motion, to sum frames with and without dose weighting, and to Fourier bin images 2 × 2 to the counting pixel size. The contrast transfer function and resolution estimates for each corrected and dose weighted micrograph was determined in cryoSPARC[61] using PatchCTF. Particles were picked in cryoSPARC v.3.2 using a Gaussian disk as a template, and subsequently processed in cryoSPARC v.3.2 as depicted in workflows shown in Supplementary Figs. 1–6.

### Model building and structure refinement

All six atomic models were built using Coot[62], PHENIX[63] and ISOLDE[64]. For the structures of $\text{apo}_{\text{wide}}$ MRP4, $\text{apo}_{\text{narrow}}$ MRP4 and ATP-bound $\text{MRP4}_{\text{E1202Q}}$, transmembrane helices and linkers were manually built in Coot using the output densities from DeepEMhancer[65]. The NBD models of the closely related bovine MRP1 (PDB 6BHU), with residues mutated to those of MRP4 via Modeller, were initially used to build the NBDs of ATP-bound $\text{MRP4}_{\text{E1202Q}}$. The final ATP-bound MRP4 NBDs were used to guide model building of the NBDs of $\text{apo}_{\text{wide}}$, $\text{apo}_{\text{narrow}}$ and all three substrate-bound structures, first by rigid-body fitting in ChimeraX, followed by real-space refinement in PHENIX and further correction in Coot and ISOLDE. All three substrate-bound states were built by rigid-body fitting individual domains of $\text{apo}_{\text{wide}}$ MRP4 into the output densities from DeepEMhancer and following the steps as above for NBDs.

The deposited $\text{apo}_{\text{narrow}}$ MRP4 model contains residues 48–398, 408–615, 692–745 and 756–1298. The deposited $\text{apo}_{\text{wide}}$ MRP4 model contains residues 48–398, 408–615, 692–745 and 756–1298. The deposited $PGE_1$-bound MRP4 model contains residues 23–394, 409–615, 693–745 and 756–1298, as well as a one $PGE_1$ and one water molecule. The deposited $PGE_2$-bound MRP4 model contains residues 46–394, 409–615, 693–745 and 756–1298, as well as one $PGE_2$ and one water molecule. The deposited DHEA-S-bound MRP4 model contains residues 10–398, 409–615, 693–745 and 756–1298, as well as one DHEA-S and three water molecules. The deposited ATP-bound $\text{MRP4}_{\text{E1202Q}}$ model contains residues 48–394, 408–615, 696–746, 756–882 and 898–1298 as well as two bound ATP, two $Mg^{2+}$ ions and a phosphatidylethanolamine lipid molecule. All models were validated against the sharpened densities from cryoSPARC. Visualizations and figures were prepared using UCSF Chimera[66], ChimeraX and Inkscape software. Cavity calculations were made with MOLEonline[67] and the 3V Server[68]. Two-dimensional diagrams of ligand–protein interactions were produced using LigPlot+[69]. *Q* scores[70] were determined in ChimeraX.

### Reporting summary

Further information on research design is available in the Nature Portfolio Reporting Summary linked to this article.

## Data availability

All five three-dimensional cryo-EM density maps have been deposited to the Electron Microscopy Data Bank (EMDB) under accession numbers EMD-40829 ($\text{apo}_{\text{wide}}$ MRP4), EMD-40828 ($\text{apo}_{\text{narrow}}$ MRP4), EMD-40827 ($PGE_1$-bound MRP4), EMD-40830 ($PGE_2$-bound MRP4), EMD-40826 (DHEA-S-bound MRP4) and EMD-40821 (ATP-bound $\text{MRP4}_{\text{E1202Q}}$). The coordinates for the atomic models have been deposited in the Protein Data Bank (PDB) under accession numbers 8SXA ($\text{apo}_{\text{wide}}$ MRP4), 8SX9 ($\text{apo}_{\text{narrow}}$ MRP4), 8SX8 ($PGE_1$-bound MRP4), 8SXB ($PGE_2$-bound MRP4), 8SX7 (DHEA-S-bound MRP4) and 8SWN (ATP-bound $\text{MRP4}_{\text{E1202Q}}$). See Table 1 for more details. Source data are provided with this paper.

## References

59. Barnett, R. E. Effect of monovalent cations on the ouabain iniibition of the sodium and potassium ion activated adenosine triphosphatase. *Biochemistry* **9**, 4644–4648 (1970).
60. Zheng, S. Q. et al. MotionCor2: anisotropic correction of beam-induced motion for improved cryo-electron microscopy. *Nat. Methods* **14**, 331–332 (2017).
61. Punjani, A., Rubinstein, J. L., Fleet, D. J. & Brubaker, M. A. cryoSPARC: algorithms for rapid unsupervised cryo-EM structure determination. *Nat. Methods* **14**, 290–296 (2017).
62. Emsley, P., Lohkamp, B., Scott, W. G. & Cowtan, K. Features and development of Coot. *Acta Crystallogr. D. Biol. Crystallogr.* **66**, 486–501 (2010).
63. Adams, P. D. et al. PHENIX: a comprehensive Python-based system for macromolecular structure solution. *Acta Crystallogr. D. Biol. Crystallogr.* **66**, 213–221 (2010).
64. Croll, T. I. ISOLDE: a physically realistic environment for model building into low-resolution electron-density maps. *Acta Crystallogr. D. Struct. Biol.* **74**, 519–530 (2018).
65. Sanchez-Garcia, R. et al. DeepEMhancer: a deep learning solution for cryo-EM volume post-processing. *Commun. Biol.* **4**, 874 (2021).
66. Pettersen, E. F. et al. UCSF Chimera–a visualization system for exploratory research and analysis. *J. Comput. Chem.* **25**, 1605–1612 (2004).
67. Pravda, L. et al. MOLEonline: a web-based tool for analyzing channels, tunnels and pores (2018 update). *Nucleic Acids Res.* **46**, W368–W373 (2018).
68. Voss, N. R. & Gerstein, M. 3V: cavity, channel and cleft volume calculator and extractor. *Nucleic Acids Res.* **38**, W555–W562 (2010).
69. Laskowski, R. A. & Swindells, M. B. LigPlot+: multiple ligand-protein interaction diagrams for drug discovery. *J. Chem. Inf. Model.* **51**, 2778–2786 (2011).
70. Pintilie, G. et al. Measurement of atom resolvability in cryo-EM maps with Q-scores. *Nat. Methods* **17**, 328–334 (2020).

## Acknowledgements

We thank P. Nguyen for assistance with virus production and D. Asarnow for discussions regarding purification and reconstitution of MRP4. This work was supported by the National Institutes of Health (NIH) National Institute of General Medical Sciences (grants NIGMS GM24485 to R.M.S. and R35GM140847 to Y.C.). R.B. was supported in part by American Heart Association postdoctoral fellowship award 9POST34370101. Mass spectrometry was performed in the UCSF Mass Spectrometry facility supported by NIH grant P41 GM103481. We thank D. P. Bulkley, G. Gilbert and M. Harrington for support with cryo-EM data collection. All data were collected at the UCSF cryo-EM facility, which is supported by NIH grants S10OD020054, S10OD021741 and S10OD026881.

## Author contributions

R.M.S., D.L.K., C.S.C., Y.C. and A.S. conceived this work. S.P., R.B. and G.M.K. expressed and functionally characterized proteins. S.P., E.G. and M.G. collected and processed cryo-EM data. S.P. and E.G. performed model building and refinement. S.P., R.B., E.G., I.E.C., R.M.S. and D.L.K. wrote the manuscript with contributions from all other authors.

## Competing interests

The authors declare no competing interests.

## Additional information

**Extended data** is available for this paper at https://doi.org/10.1038/s41594-023-01176-4.

**Supplementary information** The online version contains supplementary material available at https://doi.org/10.1038/s41594-023-01176-4.

**Correspondence and requests for materials** should be addressed to Deanna L. Kroetz or Robert M. Stroud.

**Peer review information** *Nature Structural & Molecular Biology* thanks Kenneth Linton and the other, anonymous, reviewer(s) for their contribution to the peer review of this work. Primary Handling Editor: Katarzyna Ciazynska, in collaboration with the *Nature Structural & Molecular Biology* team.

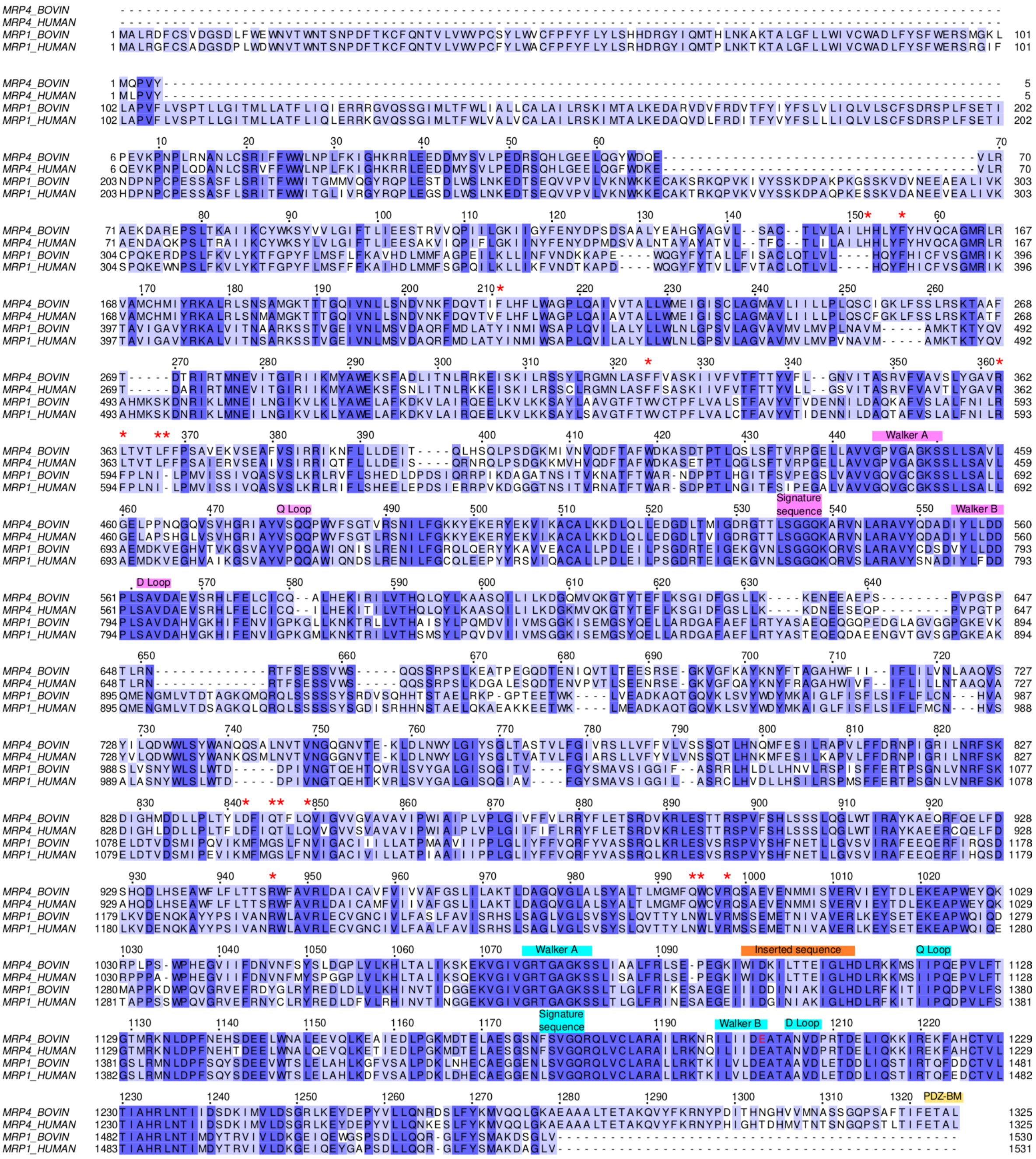

**Extended Data Fig. 1 | Sequence alignment of MRP4 and MRP1 homologs.** Sequences of bovine and human MRP4 are aligned to reflect sequence conservation across evolution and similarity to the closely related MRP1. All references to MRP4 used throughout the text refer to the bovine sequence. The residue numbers for bovine MRP4 are indicated above the sequences. Red asterisks denote a residue involved in binding one of either DHEA-S, PGE1, or PGE2. Text boxes refer to conserved sequence motifs from NBD1 (pink) and NBD2 (cyan), NBD2's inserted sequence (orange) and the C-terminal PDZ-binding motif (PDZ-BM, sand). Bovine MRP4 catalytic residue E1202 is highlighted in red.

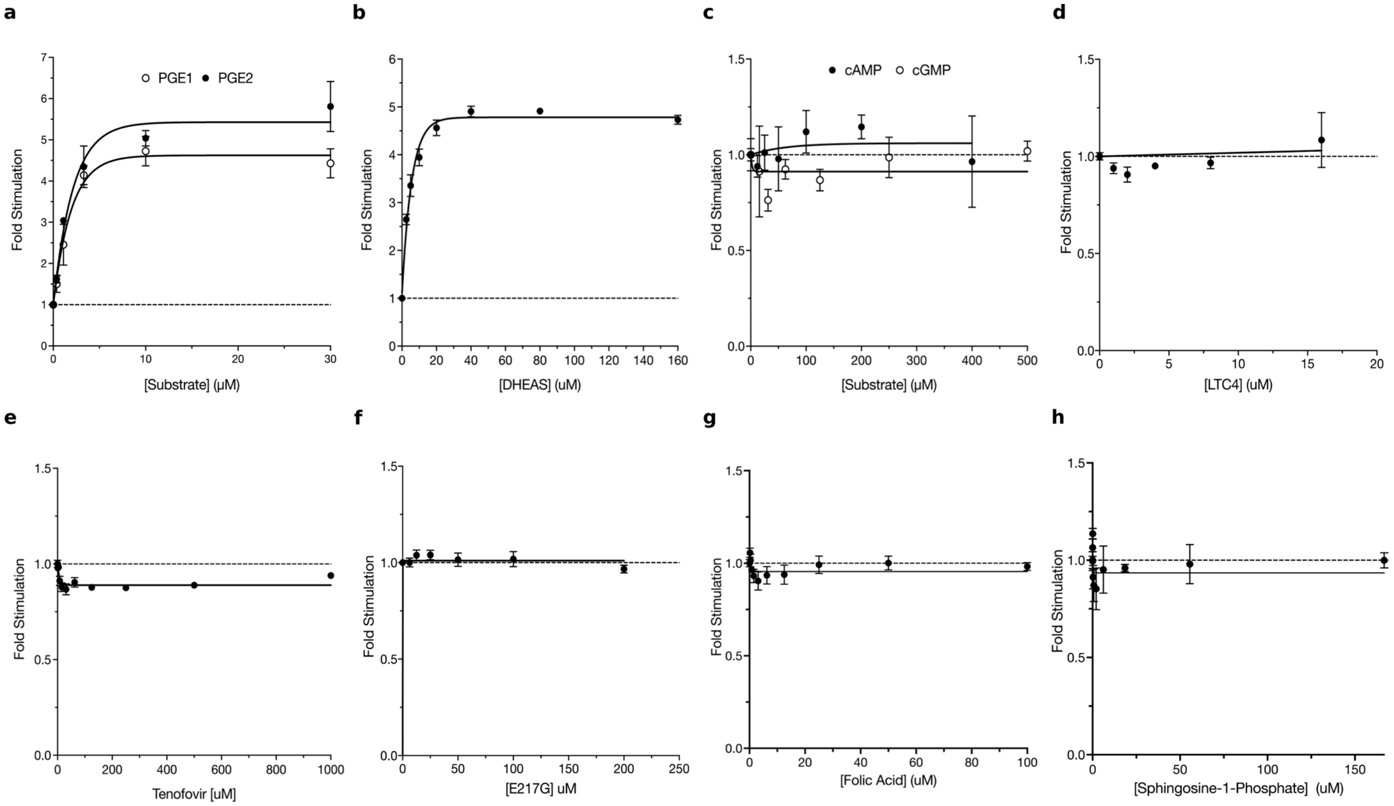

**Extended Data Fig. 2 | Biochemical characterization of MRP4.** Fold change in ATPase activity relative to basal levels with the addition of increasing concentrations of **a**, $PGE_1$, $PGE_2$, **b**, DHEAS, **c**, cAMP, cGMP, **d**, $LTC_4$, **e**, tenofovir, **f**, E217G, **g**, folic acid, **h**, S1P. Data in each panel were obtained from separate preparations of MRP4 in MSP lipid nanodisc. The basal ATPase specific activity across the samples used in panels **a**-**f** was 13.6 ± 4.5 nmol $min^{-1}$ $mg^{-1}$ from 10 biological replicates. $PGE_1$, prostaglandin $E_1$; $PGE_2$, prostaglandin $E_2$; cAMP, cyclic adenosine monophosphate; cGMP, cyclic guanosine monophosphate; $LTC_4$, leukotriene $C_4$; DHEA-S, dehydroepiandrosterone sulfate; E217G, β-estradiol-17β-D-glucuronide; S1P, sphingosine-1-phosphate.

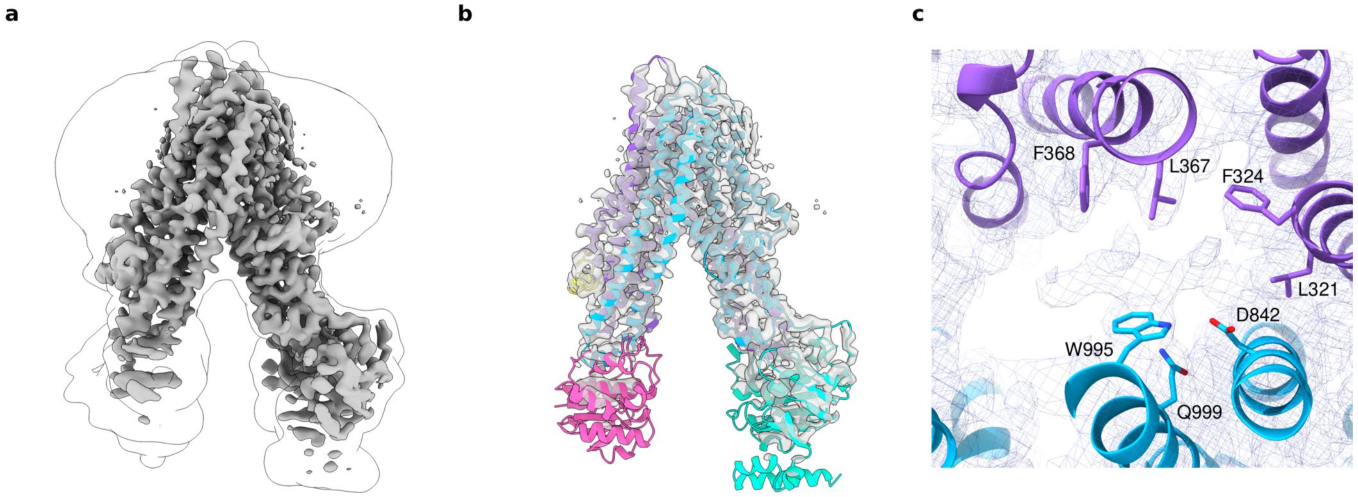

**Extended Data Fig. 3 | cAMP does not elicit a conformational change in MRP4 in cryo-EM. a** Final density of MRP4 in the presence of 1 mM cAMP from cryoSPARC. Sharpened output volume in gray, lowpass filtered volume showing the nanodisc and NBDs as black silhouette. **b** Rigid body fitting of apo MRP4 into density obtained in the presence of 1 mM cAMP. Density in gray, MRP4 domains colored as before. **c** View of substrate binding residues of the rigid-body fit apo MRP4 model in the density obtained for MRP4 in the presence of 1 mM cAMP. Map contoured at low threshold, revealing non-protein density similar to our apo MRP4 refinement. Density in purple mesh, MRP4 domains colored as before.

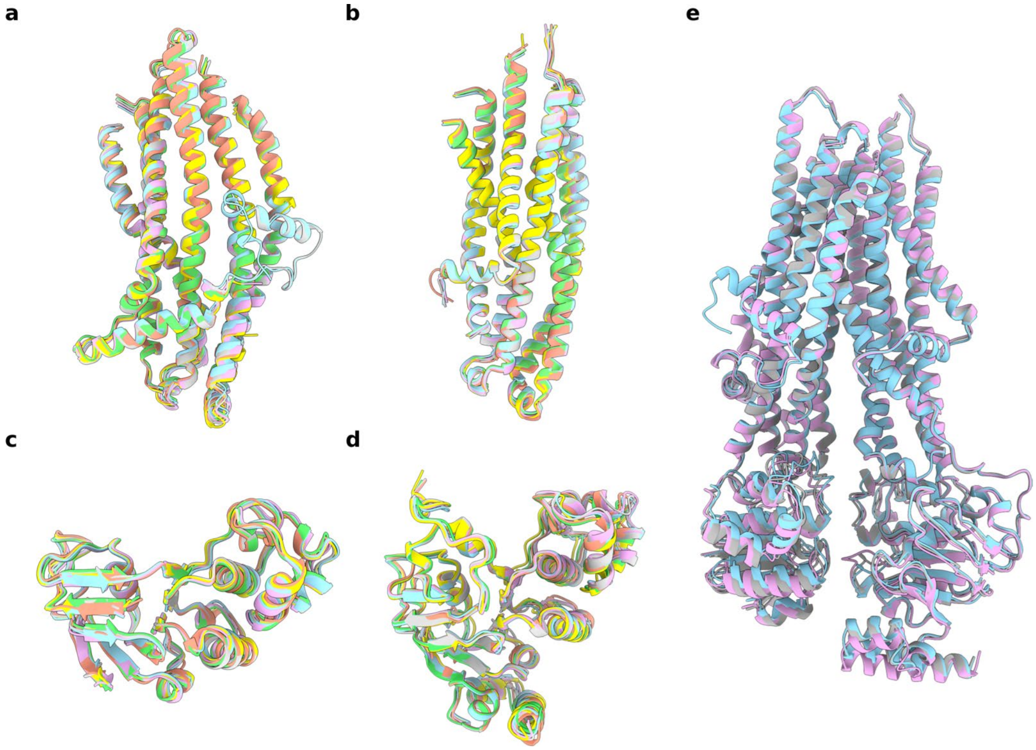

**Extended Data Fig. 4 | The domains of MRP4 move as rigid bodies throughout the substrate transport cycle.** Superposition of **a**, bundle 1 (TMs 1, 2, 3, 6, 10, 11) **b**, bundle 2 (TMs 4, 5, 7, 8, 9, 12) **c**, NBD1 and **d**, NBD2 across all five structures. Apo$_{wide}$ MRP4 in salmon, apo$_{narrow}$ MRP4 in green, DHEA-S-bound MRP4 in cyan, PGE$_1$-bound MRP4 in grey, PGE$_2$-bound MRP4 in pink, ATP-Mg$^{2+}$-bound MRP4 in yellow. **e**, Superposition of the three substrate-bound structures reveals them to share an inward-open, narrow conformation. RMSD between all Cα of DHEA-S-bound MRP4 and PGE1-bound MRP4 is 1.2 Å; between DHEA-S-bound and PGE2-bound is 0.87 Å; between PGE1-bound and PGE2-bound is 0.90 Å. Structures are colored as in **a**-**d**.

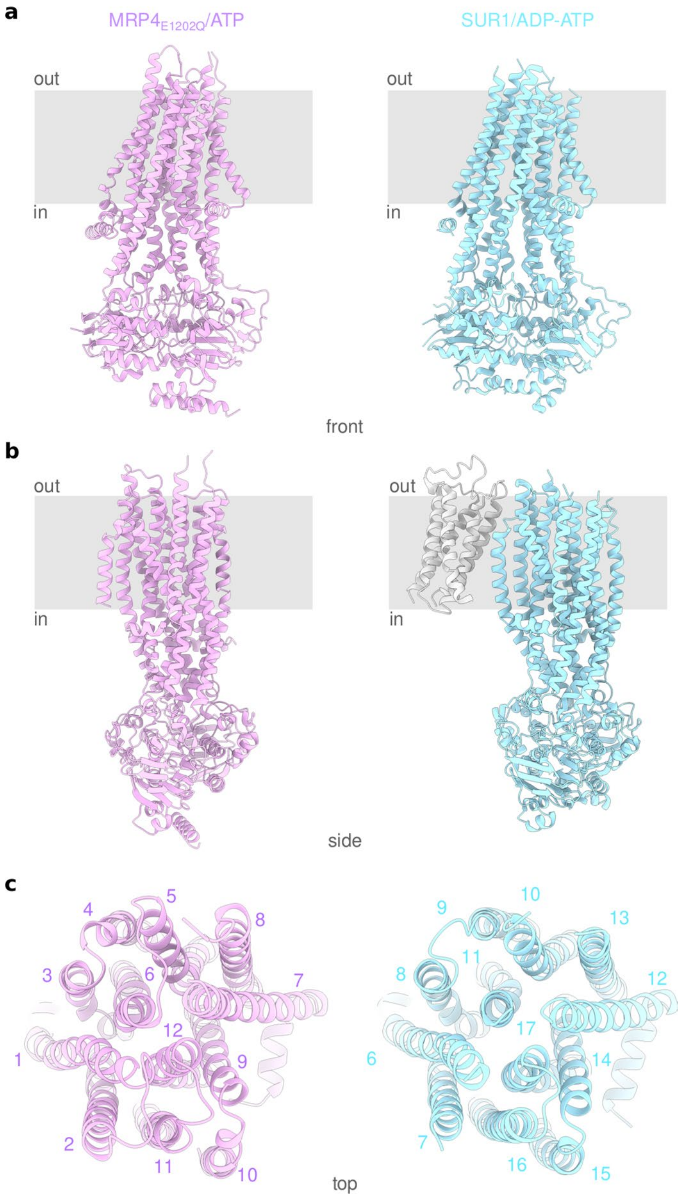

**Extended Data Fig. 5 | The outward-facing occluded state of MRP4 closely resembles the structure of SUR1 bound to ADP/ATP.** **a** Front view, **b** side view, and **c** top view of MRP4$_{E1202Q}$ bound to ATP-Mg$^{2+}$ and SUR1 bound to ADP-ATP (shown as single chain from PDB ID:6C3O). TMD$_0$ domain in SUR1 is hidden for clarity in **a** and **c**. Cα RMSD between our ATP-bound structure and SUR1 with TMD$_0$ domain deleted is 4.36 Å. MRP4$_{E1202Q}$ bound to ATP-Mg$^{2+}$ in pink, SUR1 bound to ADP-ATP in cyan, TMD$_0$ domain in light gray.

**Extended Data Table 1 | Kinetic parameters for ATPase activity of MRP4**

| Condition | $K_m$ (µM) (95% CI) | $V_{max}$ (nmol min$^{-1}$ mg$^{-1}$) (95% CI) | Maximal Fold Change |
|---|---|---|---|
| MRP4 + $PGE_1$ | 1.37 (0.84-2.28) | 57.76 (49.38-66.16) | 4.14 |
| MRP4 + $PGE_2$ | 1.68 (1.15-2.52) | 57.97 (52.27-63.70) | 5.05 |
| MRP4 + DHEAS | 2.32 (1.60-3.2) | 113.1 (106.6-119.9) | 4.78 |
| MRP4 + $LTC_4$ | NA | NA | 1.01 |
| MRP4 + $E_2$17G | NA | NA | 1.01 |
| MRP4 + cAMP | NA | NA | 1.07 |
| MRP4 + cGMP | NA | NA | 0.95 |

ATPase activity in the presence of increasing concentrations of the indicated compounds was fitted to a Michaelis–Menten equation. The kinetic parameters are mean values from at least three replicate experiments with 95% confidence intervals (CI). NA, not applicable.

nature portfolio

Corresponding author(s): Dr. Robert Stroud
Dr. Deanna Kroetz

Last updated by author(s): Oct 9, 2023

# Reporting Summary

Nature Portfolio wishes to improve the reproducibility of the work that we publish. This form provides structure for consistency and transparency in reporting. For further information on Nature Portfolio policies, see our Editorial Policies and the Editorial Policy Checklist.

## Statistics

For all statistical analyses, confirm that the following items are present in the figure legend, table legend, main text, or Methods section.

n/a | Confirmed

☐ ☒ The exact sample size (*n*) for each experimental group/condition, given as a discrete number and unit of measurement

☒ ☐ A statement on whether measurements were taken from distinct samples or whether the same sample was measured repeatedly

☒ ☐ The statistical test(s) used AND whether they are one- or two-sided
*Only common tests should be described solely by name; describe more complex techniques in the Methods section.*

☒ ☐ A description of all covariates tested

☒ ☐ A description of any assumptions or corrections, such as tests of normality and adjustment for multiple comparisons

☐ ☒ A full description of the statistical parameters including central tendency (e.g. means) or other basic estimates (e.g. regression coefficient) AND variation (e.g. standard deviation) or associated estimates of uncertainty (e.g. confidence intervals)

☒ ☐ For null hypothesis testing, the test statistic (e.g. *F*, *t*, *r*) with confidence intervals, effect sizes, degrees of freedom and *P* value noted
*Give P values as exact values whenever suitable.*

☒ ☐ For Bayesian analysis, information on the choice of priors and Markov chain Monte Carlo settings

☒ ☐ For hierarchical and complex designs, identification of the appropriate level for tests and full reporting of outcomes

☒ ☐ Estimates of effect sizes (e.g. Cohen's *d*, Pearson's *r*), indicating how they were calculated

*Our web collection on statistics for biologists contains articles on many of the points above.*

## Software and code

Policy information about availability of computer code

| | |
|---|---|
| Data collection | SerialEM 4.0 |
| Data analysis | CryoSPARC v3.2, Chimera v1.15, ChimeraX v1.5, ISOLDE v1.4, Phenix v1.20.1-4489, Coot v0.9.6, MOLE v2, DeepEMhancer v0.14, 3V, LigPlot+, Inkscape 1.02 |

For manuscripts utilizing custom algorithms or software that are central to the research but not yet described in published literature, software must be made available to editors and reviewers. We strongly encourage code deposition in a community repository (e.g. GitHub). See the Nature Portfolio guidelines for submitting code & software for further information.

## Data

Policy information about availability of data

All manuscripts must include a data availability statement. This statement should provide the following information, where applicable:

- Accession codes, unique identifiers, or web links for publicly available datasets
- A description of any restrictions on data availability
- For clinical datasets or third party data, please ensure that the statement adheres to our policy

All five three-dimensional cryo-EM density maps have been deposited to the Electron Microscopy Data Bank under accession numbers EMD-40829 (apowide MRP4), EMD-40828 (aponarrow MRP4), EMD-40827 (PGE1-bound MRP4), EMD-40830 (PGE2-bound MRP4), EMD-40826 (DHEA-S-bound MRP4), and EMD-40821 (ATP-bound MRP4E1202Q). The coordinates for the atomic models have been deposited in the Protein Data Bank under accession numbers 8SXA (apowide MRP4), 8SX9 (aponarrow MRP4), 8SX8 (PGE1-bound MRP4), 8SXB (PGE2-bound MRP4), 8SX7 (DHEA-S-bound MRP4), and 8SWN (ATP-bound MRP4E1202Q). See Table 1 for more details. Data for ATPase assays and SEC run provided as Source Data files. PDBs 6BHU and 6C3O were used in this study

## Human research participants

Policy information about studies involving human research participants and Sex and Gender in Research.

| | |
|---|---|
| Reporting on sex and gender | N/A |
| Population characteristics | N/A |
| Recruitment | N/A |
| Ethics oversight | N/A |

Note that full information on the approval of the study protocol must also be provided in the manuscript.

# Field-specific reporting

Please select the one below that is the best fit for your research. If you are not sure, read the appropriate sections before making your selection.

☒ Life sciences ☐ Behavioural & social sciences ☐ Ecological, evolutionary & environmental sciences

For a reference copy of the document with all sections, see nature.com/documents/nr-reporting-summary-flat.pdf

# Life sciences study design

All studies must disclose on these points even when the disclosure is negative.

| | |
|---|---|
| Sample size | For each of the six reported structures, several million particle images were combined through standard CryoEM analysis pipelines. Initial particles were picked using a Gaussian based particle picking template. Sample sizes were reduced by selecting classes from 2D and 3D that converged onto coherent volumes, while discarding noise and junk classes by visual inspection and FSC calculations. Resulting final volumes used for model building contain 10,000s to 100,000s of particles. |
| Data exclusions | The cryoEM processing pipeline classifies the millions of particle picks into 2D and 3D classes at various stages. Particles in either 2D or 3D classes that do not have suitable resolution, or are visually determined to be 'junk,' are excluded from further processing. Extensive cryoEM processing pipeline details are available in Supplementary Figures 3-7 and Supplementary Table 1. |
| Replication | All MRP4 ATPase activity data was done in technical triplicate. Experiments were not repeated outside of presented data, and were run independently for each substrate. |
| Randomization | Particles were assigned to random classes during heterogeneous refinement in cryoSPARC, following standard cryoEM processing protocols. Final reported cryoEM volumes use full particle image set assigned to that volume. |
| Blinding | No blinding was used in this study, following standard cryoEM analysis pipelines. |

# Reporting for specific materials, systems and methods

We require information from authors about some types of materials, experimental systems and methods used in many studies. Here, indicate whether each material, system or method listed is relevant to your study. If you are not sure if a list item applies to your research, read the appropriate section before selecting a response.

## Materials & experimental systems

| n/a | Involved in the study | |
|---|---|---|
| ☒ | ☐ | Antibodies |
| ☐ | ☒ | Eukaryotic cell lines |
| ☒ | ☐ | Palaeontology and archaeology |
| ☒ | ☐ | Animals and other organisms |
| ☒ | ☐ | Clinical data |
| ☒ | ☐ | Dual use research of concern |

## Methods

| n/a | Involved in the study | |
|---|---|---|
| ☒ | ☐ | ChIP-seq |
| ☒ | ☐ | Flow cytometry |
| ☒ | ☐ | MRI-based neuroimaging |

## Eukaryotic cell lines

Policy information about cell lines and Sex and Gender in Research

| | |
|---|---|
| Cell line source(s) | SF9 cells. The Sf9 insect cell line is a clonal isolate derived from IPLB-Sf-21-AE. Purchased from Expression Systems. |
| Authentication | Commercial purchase - no authentication was used. |
| Mycoplasma contamination | Not tested for mycoplasma contamination. |
| Commonly misidentified lines<br>(See ICLAC register) | *Name any commonly misidentified cell lines used in the study and provide a rationale for their use.* |